
High temperature Tensile test of 12Cr ferritic ODS steel

POLYTECHNIC OF TURIN

Department of Energetic Engineering

UNIVERSITY OF TOKYO

Nuclear Engineering and Management department

MASTER THESIS

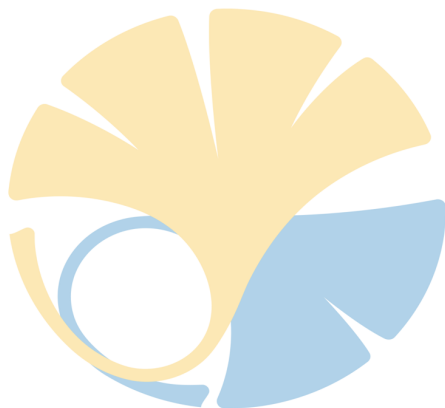
By

Meli Antonino

supervised by

Pr. Massimo ZUCCHETTI

Pr. Hiroaki ABE



東京大学
THE UNIVERSITY OF TOKYO

October 11, 2018



ABSTRACT

The ODS steel, studied for more than thirty years, is an alloy characterized by very high performances, and depending on the purpose, its composition is changed in order to satisfy the requirements. In particular, the 12Cr ferritic ODS steel is widely regarded as a candidate structural material for fusion reactor and advanced next generation reactors. In this study, mechanical properties of the alloy will be tested at different temperatures: their dependency on the microstructure and on the temperature will be investigated, focusing the attention on the anisotropy of the alloy and how it affects its performances. Fracture surface analysis at room temperature will be also performed.

AUTHOR'S DECLARATION

I declare that the work in this document was carried out in accordance with the requirements of the University's Regulations and Code of Practice for Research Degree Programmes and that it has not been submitted for any other academic award. Except where indicated by specific reference in the text, the work is the candidate's own work. Work done in collaboration with, or with the assistance of, others, is indicated as such. Any views expressed in the dissertation are those of the author.

SIGNED: DATE:

DEDICATION AND ACKNOWLEDGEMENTS

This one year journey was mainly characterized by the study of my master thesis. It was not a simple path, maybe because it was my first experience of research, but it gave me the opportunity to grow and to make something I think hardly I would have made in my own university.

I would like to thank my thesis advisor, the Professor M. Zucchetti of the Department of Energetic Engineering at the Polytechnic of Turin. He accepted to help me during my work, and his advices were helpful.

I would like to thank my supervisor, the Professor Hiroaki Abe of the Nuclear Engineering and Management department of the University of Tokyo. The door of his office was always open whenever I needed of some advices, or expert's opinion; he allowed this paper to be my own work, but steered me in the right direction every time he thought I needed it.

I must to thank also the Doctor Jingjie Shen of the National Institute of Fusion Science and the Doctor Huilong Yang of the University of Tokyo. They assisted me whenever it was necessary, teaching me the fundamentals of the experimental research. I know for sure that without them it would have been definitely harder.

I need to express my very profound gratitude to my parents for giving me their support not only during this year, but during all my university career. This accomplishment would not have been possible without them. Finally I feel to mention some of my friends which supported me in the hardest moments, and

cheer with me in the moments of happiness: Martina, Fede, Claudia, Chiara, Andre, Mello, Ricky, Edoardo, Dionisio, Matte, Francesco and my brother, Biagio.

Contents

1	Introduction	1
1.1	Nuclear Energy	2
1.1.1	Fission plants	2
1.1.2	Fusion reactor	4
1.2	Oxide Dispersed Steel (ODS)	8
1.2.1	Fabrication process	8
1.2.2	Anisotropy of the microstructure	11
1.2.3	Tensile and creep properties at high temperatures	12
1.2.4	Irradiation effect on ODS steel	15
1.2.5	Microstructural stability	15
1.3	Aim of this thesis	17
2	Experiments	18
2.1	Material	18
2.1.1	Sample preparation	18
2.2	Microstructural and Mechanical characterization	20
3	Results	22
4	Discussion	26
4.1	Microstructure	26
4.2	Strengthening mechanism	28
4.2.1	Room temperature analysis of the strengthening mechanisms, and comparison with experimental results	32
4.2.2	High temperature analysis of the strengthening mechanisms	34

4.3	Total elongation and fracture surface	42
4.3.1	Total elongation analysis	42
4.3.2	Fracture surface analysis	42
5	Conclusions	50

List of Figures

1	Evolution of the nuclear plant design [1]	4
2	Fusion cross section for the main reaction in function of the energy of the reacting particles [6]	5
3	Schematic of the Tokamak model of fusion reactor in construction, ITER [5]	6
4	Manufacturing process of 12Cr ODS ferritic steel cladding [18]	10
5	(5a) DBTT trends of the alloy on all the three direction [22]; (5b) Cold rolling process and heat annealing for increase of the hardness [18].	11
6	Comparison on the yield stress of some experimental alloys and some already commercialized with one alloy with no nanoparticles in the microstructure [15]	13
7	Creep comparison among various alloys [15]	14
8	Original matrix shape	19
9	SSJ-type tensile specimen: 16x4x0.25 mm	19
10	Experimental results of the tensile tests	23
11	Comparison about yield stress and UTS	24
12	Comparison about total elongation	25
13	Inverse Pole Figure (IPF) of the microstructure	27
14	EPMA elemental mapping of coarse precipitates [36]	28
15	Schmid analysis for the RD sample	33
16	Schmid analysis for the TD sample	34
17	Schematic representation of the Friedel effect (upper sequence – shearing of precipitations) and of the Orowan mechanism (lower sequence – bow-out between precipitations)	36

19	Results obtained during the heat treatments performed in the study of Shen et al. [68]	37
18	Orowan mechanism: governing behaviors of the precipitation hardening [75]	38
20	Normalised stress $\frac{\sigma}{\tau}$ as a function of temperature as predicted by a Discrete-Obstacle model – dashed – and two collective models, Butt-Feltham – dotted – [73] and Kocks – solid line – [69]	39
21	Fracture analysis of the samples – Necking process	44
22	Secondary crack on the TD sample – zoom 1.	45
23	Fracture analysis of the samples – low magnification	46
24	Fracture analysis of the samples – medium magnification	47
25	Fracture analysis of the samples – high magnification	48

List of Tables

1	Reactor core conditions and material for Gen IV design [2] FM: ferritic martensitic stainless steel, ODS: oxide dispersion strengthened steels	3
2	Candidate materials for first wall blanket and inner components [8]	7
3	Weight% of the elements in the ODS steels composition [15]	9
4	Chemical composition of the 12Cr ODS steel in weight percentage [43]	18
5	Theoretical [65] and experimental values of the Young's modulus	21
6	Experimental values of yield stress , UTS and total elongation – RD samples – TD samples	24
7	Experimental and calculated yield stress [MPa] at RT	32

1 Introduction

The energy has a very key role in our every day's life. With the enhancing of the average wellness also the demand of energy rises. From the first industrial revolution the mankind had supplied to the energy demand mainly through the usage of coal and oil and in the last decades also the usage of natural gas has increased. These kinds of energy resources have some drawbacks:

- limited storage: they will exhaust within several decades, since their usage rate is definitely larger than the natural regeneration of them through transmutation of organic material in higher concentration of Carbon one.
- Among their reaction products there is the carbon dioxide, the main responsible of the global warming; plus, they also release some other reaction products which increase the pollution in the air

In the last decades many efforts have been made in order to solve the energy shortage problems enhancing the transfer efficiency of fossils fuel, and also seeking new alternative ways of producing energy, like sunlight, wind, geothermal heat, water (taking advantage of waves, tides, potential energy) etc. Nuclear energy has been considered a valid alternative for its high density power generation, its null gas emission and cost effective.

1.1 Nuclear Energy

When we talk about nuclear energy we mean the use of the nuclear reaction to produce heat to be converted in electricity afterwards; basically the nuclear reaction cause the fission of heavy atoms, or the fusion of light ones.

1.1.1 Fission plants

So far, there are more than 430 fission plants in the globe, which are able to provide $\sim 11.55\%$ of the energy world demand. In the image below 1 [1] is shown the history of the nuclear fission plants, starting from the Gen I reactors, until the today's new designs of reactors, much more efficient, economically competitive and with sensible reduction of radioactive waste production thanks also to a better usage of the fuel. In table 1 are shown the conditions the new design of reactors have to deal with, which are much more aggressive than the ones of the already existing plants. These performances could be guaranteed using material the peculiarity of which are reported below:

- Good geometry stability against thermal and irradiation creep, void swelling, etc
- Enhanced ductility, strength, creep resistance, fatigue
- High chemical inertia of the cladding and other materials with the coolant and fuel.
- Good irradiation resistance under high neutron flux, embrittlement.
- workability, economic aspects etc.

Table 1: Reactor core conditions and material for Gen IV design [2] FM: ferritic martensitic stainless steel, ODS: oxide dispersion strengthened steels

Systems	Coolant	Pressure [MPa]	T_{in}/T_{out} [K]	Neutron spectrum, maximum dose (dpa)	Cladding
GFR	Helium, supercritical CO_2	7	673/1123	Fast,80	Ceramic
LFR	Lead or Lead-Bismuth	0.1	873/1073	Fast,150	High-Si FM,ODS, ceramics, refractory alloys
MSR	Molten salt	0.1	973/1273	Thermal,200	-
SFR	Sodium	0.1	643/823	Fast,200	FM or FM ODS
SCWR	Supercritical water	25	563/873	Thermal, ~ 30 , Fast, ~ 70	FM, ODS, etc
VHTR	Helium	7	873/1273	Thermal, <20	SiC or ZrC coating and surrounding graphite

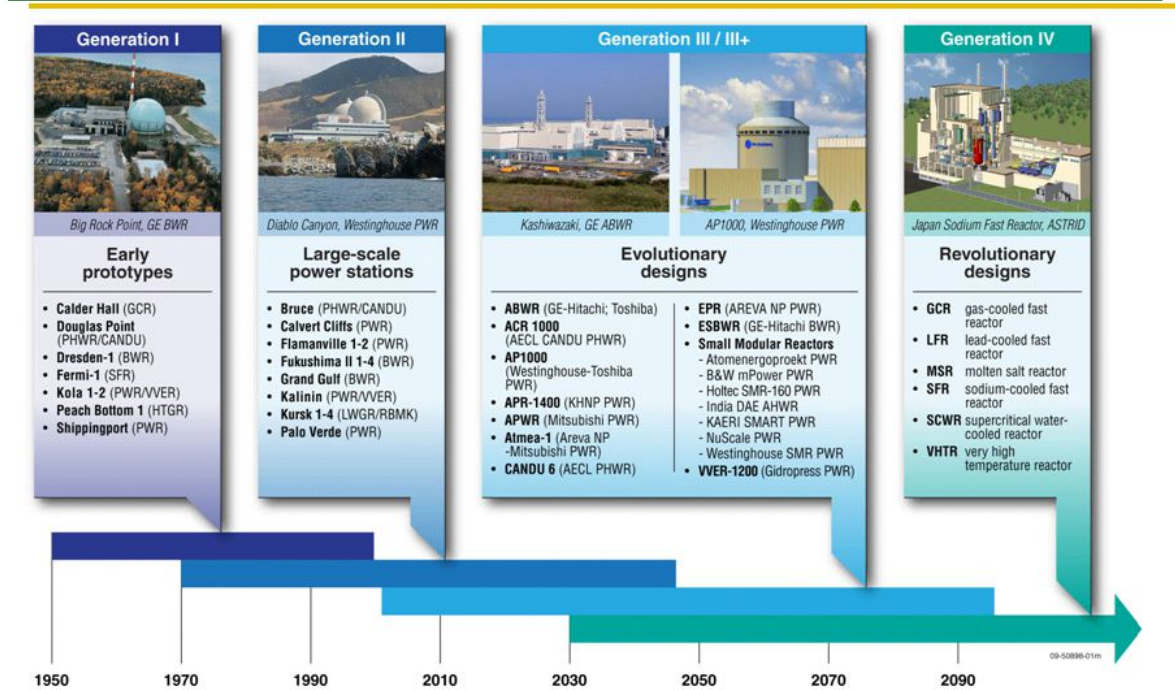


Figure 1: Evolution of the nuclear plant design [1]

1.1.2 Fusion reactor

It was said that for nuclear reaction we mean both fission and fusion reactions. The second one can likely occur with light elements rather than the heavier ones because in terms of energy gain in the first case is higher [3]. The fusion reactions studied and developed so far are related to the hydrogen isotopes [4]:





The energy gain from the reaction is partially converted in kinetic energy of the neutron/proton (the majority of that, will be converted in heat and electricity afterward) and the daughter (the remaining part, it will support the plasma).

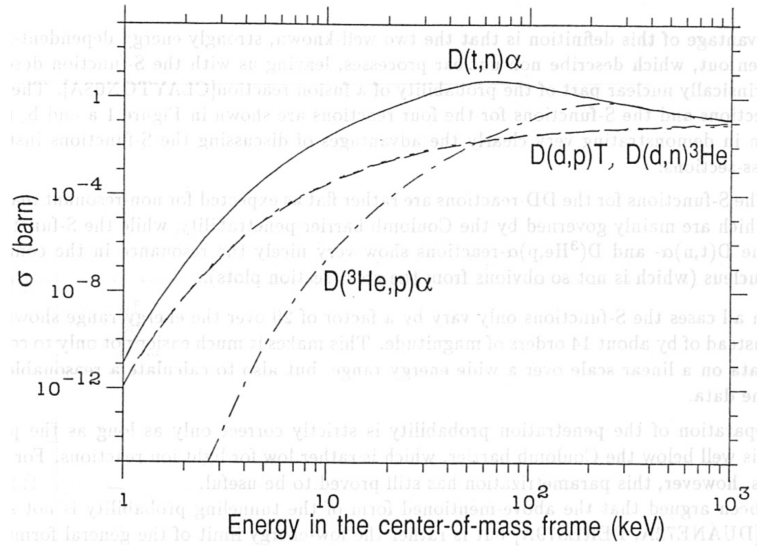


Figure 2: Fusion cross section for the main reaction in function of the energy of the reacting particles [6]

and the neutrons obtained from the reactions are absorbed by the first wall/blanket which will transfer the heat to the external circuit to produce electricity. In figure 3 is shown one of the designs developed to sustain the fusion reaction and to convert the energy from heat to electricity.

The first reaction is the one with the highest energy release, but also the most likely to occur in terms of probability cross section (figure 2) at the "lowest" temperature of almost 150 million Kelvin which correspond to an energy of the reacting particles of several keV [6]. In order to contain the matter at this state – plasma, at this temperature – a very strong magnetic field is used. The heat

THE ITER-FEAT MACHINE

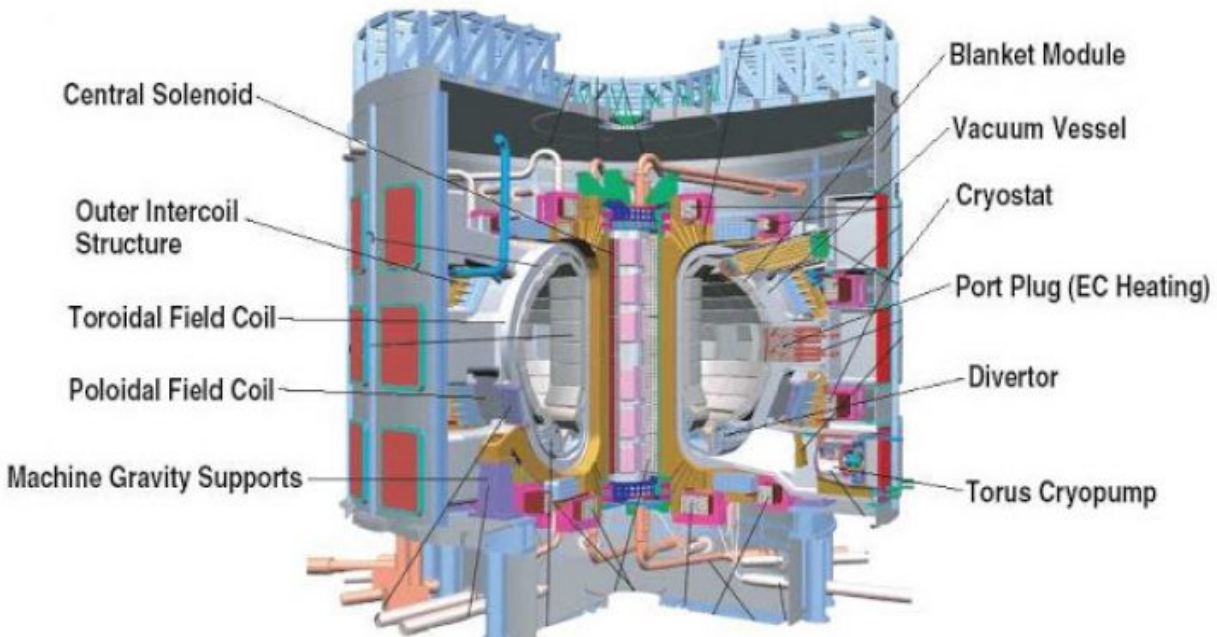


Figure 3: Schematic of the Tokamak model of fusion reactor in construction, ITER [5]

Due to the very high temperature of the plasma and the high energy of the neutrons, the blanket need to be designed in order to stand such aggressive conditions, and still be able to transfer the heat to the coolant: also in this case the materials need to have a high strength at very high temperatures, good irradiation resistance, still being able to conduct the heat (sufficiently good thermal conductivity), and also good compatibility with coolant and breeders. To satisfy all the requirements already mentioned, some advanced alloys have been studied: between them there are the Reduced Activation Ferritic (RAF) steels, the Reduced Activation Ferritic-Martensitic (RAFM) steels (including also the ODS ones), Vanadium alloys [7].

In table 2 [8] are reported the materials which should be used in the construction of the first wall and the inner components:

Table 2: Candidate materials for first wall blanket and inner components [8]

Function	First wall	Breeding blanket	Divertor
Plasma facing material	W-based alloy, W-coated ODS steel, flowing liquid metal: Li	-	W-based alloy, flowing liquid metal: Li, Ga, Sn, Sn-Li
Neutron multiplier material	-	Be, $Be_{12}Ti$, $Be_{12}V$, Pb	W-coated SiC_f/SiC
Tritium breeding material	-	Li, eutectic Pb-Li, Li-based ceramic (e.g. Li_2O , material $Li_4SiO_4 + 2.5$ wt% SiO_2 , $LiTiO_3$, Li_2ZrO_3 , $LiAlO_2$)	-
Structural material	RAFM steel, ODS steel V-based alloy SiC_f/SiC	RAFM steel, ODS steel V-based alloy, SiC_f/SiC	ODS steel, W-based alloy
Coolant	-	Water, He eutectic Pb-Li, Li	Water, He

1.2 Oxide Dispersed Steel (ODS)

1.2.1 Fabrication process

The ODS steel is a very performing alloy developed in the early 1980 with the purpose to dispose, after their usage, wastes with lower activity [11]. In order to reach that goal, elements with slow decay rate often used in the alloying process of the steel, such as Molybdenum and Niobium, have been substituted with Tungsten, Vanadium, and Titanium, obtaining still good strengthening, but with elements characterized by higher decay rate [9, 10]. The studies performed have revealed that the ductile-brittle transition temperature (DBTT) depends on the Chromium weight%, and also that the best compromise between strength and toughness has been observed occurring with a Cr weight% of 9-10% [12]. They also found out a relationship between the Tungsten content in the alloy, and the creep strength [13]: the creep strength increases quite linearly with the weight% of W up to 2%, while with higher weight% they observed a possible increase of the DBTT since some F_2W might precipitate. The alloys developed so far allowed to increase the operating temperatures up to $\sim 823K$ [14, 15]. So it was thought to add oxide particle in the alloy making it more stable, trough mechanical alloying [16] used already in the production of Ni-based alloys characterized by uniform microstructure. The research on this aspect increased rapidly, and some Ni-based and Fe-based ODS alloys have been developed: more details are shown in table 3, [15].

In their work, Ukai et al [23] studied how the addition of Ti, Ni, V and Zirconium influences the size distribution of oxide particles: the Ti addition hindered the growth of oxide particles, allowing further creep rupture strength. The creep rupture strength of ODS steel is not isotropic, since it is higher along the direction of the hot extrusion direction rather than the transversal one [23].

In figure 4 is represented the general procedure in order to obtain an ODS Steel: after being mixed together, the base powder and the nano scale oxides are milled in a can with steel ball; afterward the mixture is consolidated through hot isostatic pressing or hot extrusion (sometimes both of them).

Table 3: Weight% of the elements in the ODS steels composition [15]

Element	MA956	MA957	PM2000	12Y1	12YWT
C	0.03	0.03	0.01	0.045	0.05
Mn	0.06	0.06	0.11	0.04	0.6
P	0.008	0.007	<0.002	<0.001	0.019
S	0.005	0.006	0.0021	0.002	0.005
Ni	0.11	0.13	0.01	0.24	0.27
Cr	21.7	13.7	18.92	12.85	12.58
Mo	<0.05	0.3	0.01	0.01	0.02
Ti	0.33	0.98	0.45	0.003	0.35
Al	5.77	0.03	5.1	0.007	-
W	-	-	0.04	<0.01	2.44
N	0.029	0.044	0.0028	0.017	0.014
O	0.21	0.21	0.25	0.15	0.16
Y	0.38	0.28	0.37	0.20	0.16
Fe	balance	balance	balance	balance	balance

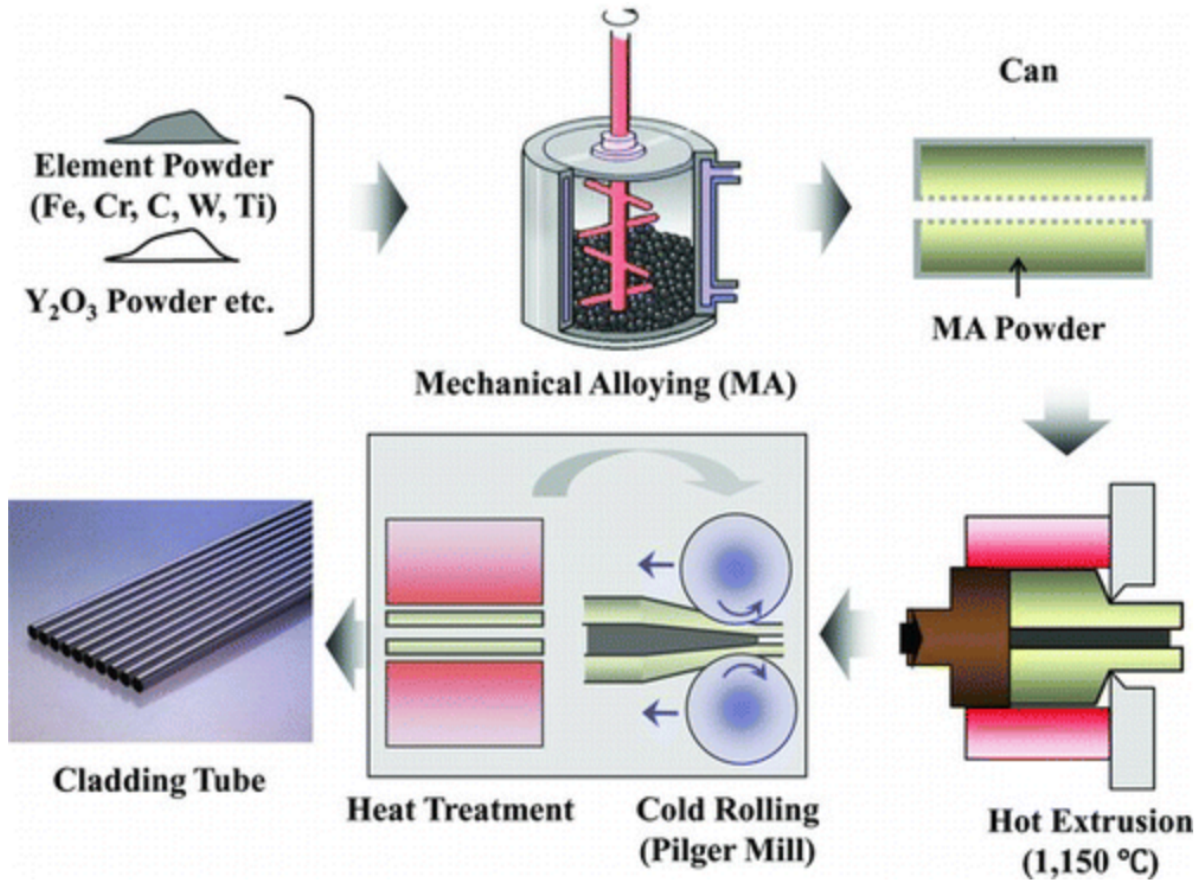


Figure 4: Manufacturing process of 12Cr ODS ferritic steel cladding [18]

As last step, the alloy is cold rolled and eventually annealed: these two steps can be repeated more than once. In their work [20], Kimura et al. figured out how the corrosion resistance at high temperature is influenced by the Cr content in the alloy: to have sufficient corrosion strength, the Cr wt% should not be lower than 12%. They also found out that above the 19% of Cr the DBTT changes significantly after aging at 873K, thus the optimum from this point of view seems to be around 14-16% of Cr in the alloy.

1.2.2 Anisotropy of the microstructure

In their work, Serrano et al. [21] studied the microstructure of the ODS steel, and observed that the grains are different between the direction along the hot extrusion and the transverse one: on the first case they were more elongate – 855nm x 533nm – while on the second one they were more uniformly shaped – 417nm x 394nm.

The tensile properties (yield stress and ultimate strength) were not so different along both the directions, the same could not be said for the hardness and the ductility: the hardness test reported 362HV in the first case and 392HV in the second case; for what concern the ductility, they found out that the alloy is definitely more ductile along the hot extrusion direction rather than the transversal one, and this might be related to the grains distribution in both the direction.

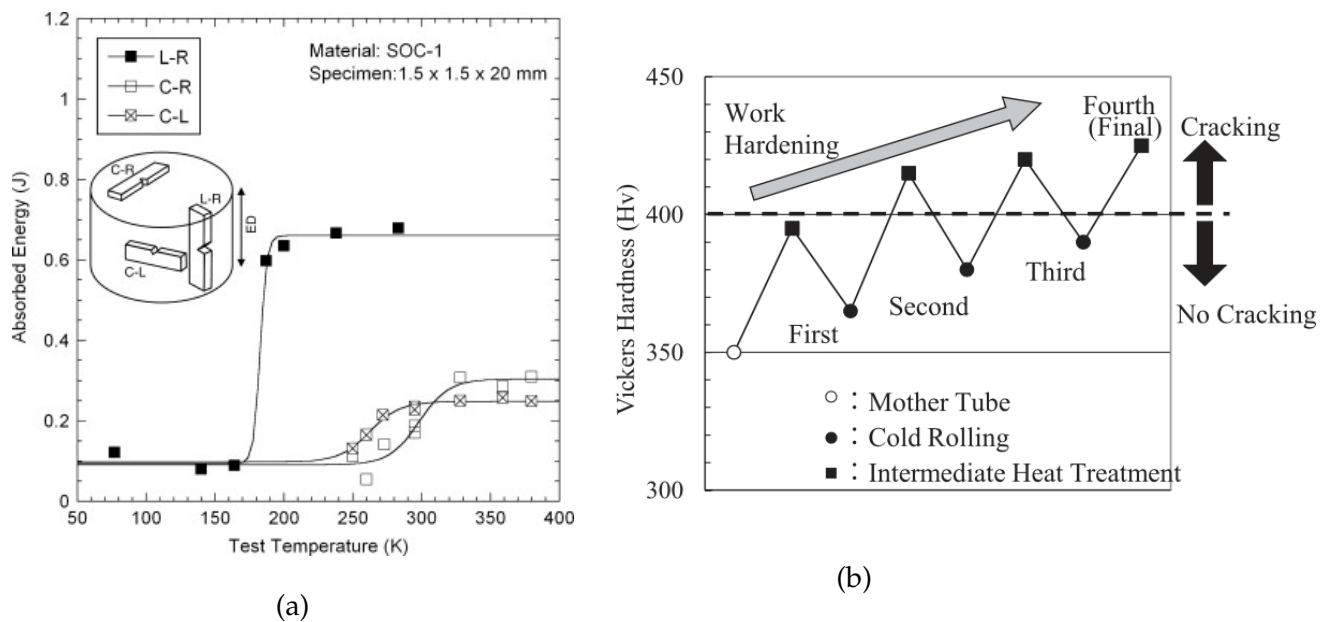


Figure 5: (5a) DBTT trends of the alloy on all the three direction [22]; (5b) Cold rolling process and heat annealing for increase of the hardness [18].

In another study the DBTT of the alloy on different direction with respect to the

hot extrusion one was investigated [22]: in the Charpy tests Kasada et al. observed a marked difference in the energy absorbed by specimen in L-R with respect to the other two direction – figure 5a – thus also the DBTT was different, since the morphology of the grains is different along the hot extrusion direction.

The anisotropy of the microstructure given by elongated grains along the hot extrusion direction, is due to the mentioned process. Nevertheless the hot extrusion process enhances the growth of elongated grains, the ODS microstructure is known to have fine grains, high density dislocations and large concentration of nano-oxide particles.

In the work of Klueh et al. [15] about the 12YWT, the dislocation density was around 10^{15} - 10^{16} , the particle size only few nm in diameter with a number density of the order of $10^{23}/m^{-3}$, characterizing the alloy with a UTS larger than 1200MPa at room temperature and a total elongation lower than 5%. Thus for this alloy it would be good to improve the ductility, using process such as the cold rolling. The cold rolling is usually coupled with a heat treatment – figure 5b [18] – since only that could enhance the formation of cracks in the alloy.

1.2.3 Tensile and creep properties at high temperatures

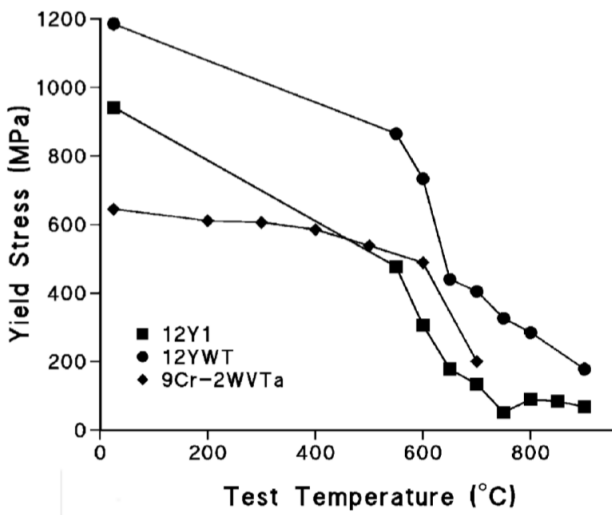
In their works, Klueh et al. [15, 24] compared the properties of some experimental and commercial ODS alloys with a non-ODS reduced activation steel – ORNL 9Cr-2WVT.

The tensile properties of the alloy without nanoparticles are lower than the ones of the 12YWT (figure 6) within the entire range of temperature studied: this is due to the Ti presence in the alloy (it leads to the Y-Ti-O complex oxides formation) and the uniform distribution of W in the microstructure – both of them increase the yield stress of the alloy. The same cannot be said for the 12Y1, performances of which drop after 600°C. For what

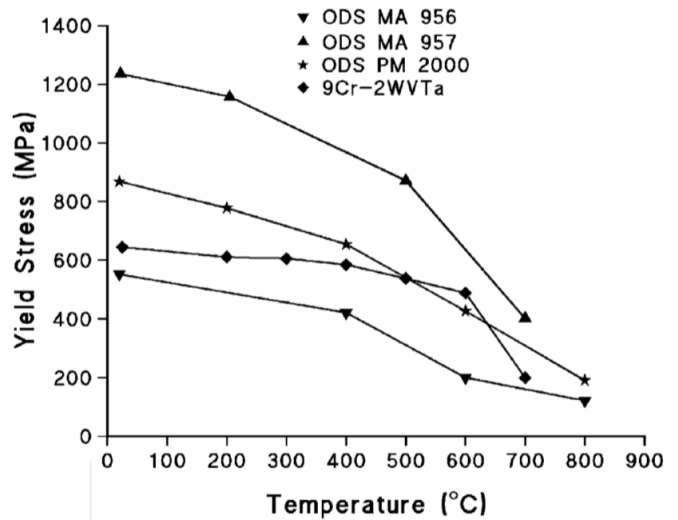
concerns the comparison with the already commercialized alloys, the MA957 has the best performances while the ORNL 9Cr-2WVT ranges between the other two trends.

Klueh et al. analyzed also the creep properties of the already mentioned alloys by means of the Larson Miller parameter (LMP, used to predict the lifetime of a material depending on the time before rupture, t_r , and the working temperature, T , as shown in the equation (4), [26]).

$$LMP = T[C + \log(t_r)] \quad (4)$$



(a) Experimental ODS steels vs steel without nanoparticles



(b) Commercial ODS steels vs steel without nanoparticles

Figure 6: Comparison on the yield stress of some experimental alloys and some already commercialized with one alloy with no nanoparticles in the microstructure [15]

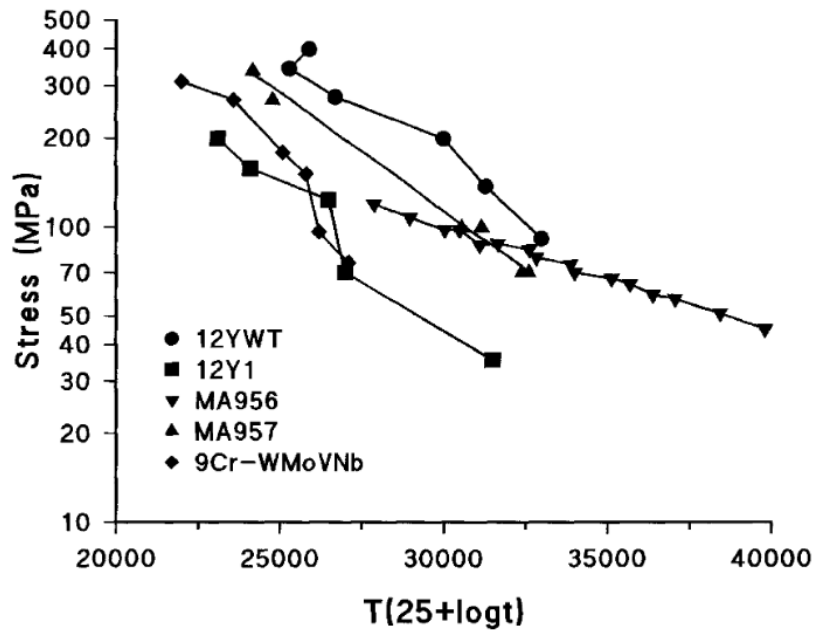


Figure 7: Creep comparison among various alloys [15]

In figure 7 are shown the trends imposing a $C=25$ [15]: the ones of the experimental alloys and of 9Cr-2WVT are pretty similar. The commercial alloys have shown similar trends with the experimental ones only at high LMP, while they seem weaker at low LMP. In their work [19], T. Hayashi et al. have analyzed the creep properties of the 14YWT at 800°C , reporting a structure composed by fine grains and good creep resistance. According to the results, it seemed no sensible sliding of grain-boundary occurred.

Brandes et al. [25] studied the microstructure of the alloy during creep experiments, and they found out that dislocation glide was the main mechanism of deformation, and that the microstructure was stable. Also, dislocation could be trapped by particles according to their interaction with nanoclusters. They have also realized how nanocluster provided enough strengthening owing to an attractive interaction with movable dislocations, thus the driver of the creep was a stress-assisted thermal activation from nanocluster traps.

1.2.4 Irradiation effect on ODS steel

Considering the purpose with which the ODS steel are developed and studied – candidate material for the cladding of new designs of fission reactors and also for the blanket of the fusion reactor – it is important to investigate their reaction under radiation. Miller et al. [27] investigated the MA957 studying how the alloy is affected by a neutron irradiation of 3dpa (displacement per atom) at 600°C though atom probe tomography: they did not find any sensible changes on the size, number density and composition of the Y-Ti-O dispersoids. In another work [28] it was observed that the He does not affect too much the creep properties of the 14CrWTi ODS steel at 650°C (only the creep rupture time has been slightly reduced).

1.2.5 Microstructural stability

We have already understood how really good are the properties of the ODS steels, and the main difference with the other steels is the presence of nanoparticles. Due to such extraordinary properties they have conferred to the steel, a lot of studies have been performed on them. They have found different types of nano-dispersoids, such as Y_2O_3 with cubic structure [29], $Y_2Ti_2O_7$ with pyrochlore one [29, 30], Y_2TiO_5 with exagonal one [31], or even orthorhombic structure [32], $YTiO_3$ [33], $TiCr_2O_4$ [34], Ti(C,O,N) [35,36] and $M_{23}C_6$ [36]. These nanoparticles are able to:

- To increase the strength of the alloy hindering the motion of dislocation and grain boundaries too.
- To absorb the irradiation effects acting as sink for point defects.
- To trap helium at the precipitate/matrix interface, and retard its formation [37, 38].

Thanks to the already mentioned dispersoids, the alloy gains toughness at low irradiation temperatures and increases its creep strength at high temperatures. According to the studies made so far the great properties of the alloy are related also to its fabrication process, which allows the formation of fine grains, high density of dislocation and nanoparticle distribution: these three factors are considered the main responsible of the performances of the alloy [38, 39, 40]. In these studies, researchers tried to develop appropriate models in order to calculate the properties of the alloy and to compare the results with the experimental data. In their work, Song et al. [38] focused their attention on the mechanism of strengthening of grain boundaries and dispersoids on a 12Cr-ODS alloy. It was also investigated the influence of the annealing process on the thermal stability of the alloy. Schneibel et al. [41] studied the 14YWT ODS steel after a heat treatment of 30h at 1273K: they found out a decrease on the density of the alloy caused by an increase in the pore formation during the annealing. Some others did not observed any significant change on the motion of coarse oxide particle, with the addition of Ti in the matrix subjected to an annealing treatment of 100h at 1473 K [42], and this matched with the diffusion-controlled mechanism. Some other studies have been performed, but since most of them have focused their attention on a certain annealing temperature, the coarsening kinetics was not fully studied enough, and is still a not well clear phenomenon.

1.3 Aim of this thesis

The ODS steel is a material developed to stand very aggressive conditions like those the cladding of the fuel rods has to deal with in fast breeder reactors, or the blanket in the first wall of the fusion reactor. Thus it should have very high temperature creep resistance, good irradiation resistance as well. Nevertheless, it has also to be able to absorb sufficient deformation in order to stand sharp temperature or pressure gradients than can occur during working time, thus also its ductility has to be improved.

For the already mentioned requirements, the microstructure of the alloy should have a large amount of nanoparticles and to be more or less uniformly recrystallized. Consequently the alloying process has to be designed properly, even though, some stages give to the alloy an anisotropic grain size distribution, characterized by more elongated grains along the cold rolling direction and more uniform ones on the transversal direction.

The aim of this thesis is to study the behavior of a 12Cr ferritic ODS steel – the composition of which will be shown afterwards – at different temperatures and to observe how its microstructure and the mechanical performances are affected by. Experiments at room temperature, 400°C and 600°C will be performed, and then the sample fracture surface and the data recorded by the machine will be analyzed. We need to keep in mind that the alloying process characterizes the microstructure of the alloy, and this may lead to different results of the data recorded by the machine and different fracture modality.

2 Experiments

2.1 Material

The alloy with which the samples have been made, was fabricated by KOBELCO [43] and its composition is shown in the figure 4. It was obtained through mechanical alloying of the base metal with Y_2O_3 powder in a milling attritor under argon atmosphere; the attritor worked at the speed of 250rpm for 48h. After that, the mixture was degassed for 3h at 673K in a low pressure environment($p < 0.1Pa$) and canned in mild steel. Afterward, in the consolidation process the alloy is shaped into a 30-mm diameter bar by hot extrusion at 1423 K. The bar was hot forged at 1423K into a sheet, and annealed at 1373K for 1h. As last step, the obtained sheet was cold rolled (along the same direction of the hot extrusion process) in order to reduce its thickness up to 60% and re-annealed at 1323K for 1h under air-cooling.

Table 4: Chemical composition of the 12Cr ODS steel in weight percentage [43]

Element	Cr	W	Ti	Y	C	N	Fe
Composition	12.01	1.91	0.31	0.20	0.033	0.008	balance

2.1.1 Sample preparation

From the matrix sheet dog-bone shaped tensile samples with a gauge section of 5x1.2x0.25mm have been obtained cutting it along the the rolling direction (henceforth RD) and along the

transversal direction (henceforth TD). The samples are still not ready to be used, since they need to be prepared before being tested: if they have any oxidation or scratches on their surfaces, they have to be treated with sand-paper and polished in order to make them shining and without scratches. At the end of the treatments, the sample will appear as shown in figure 9

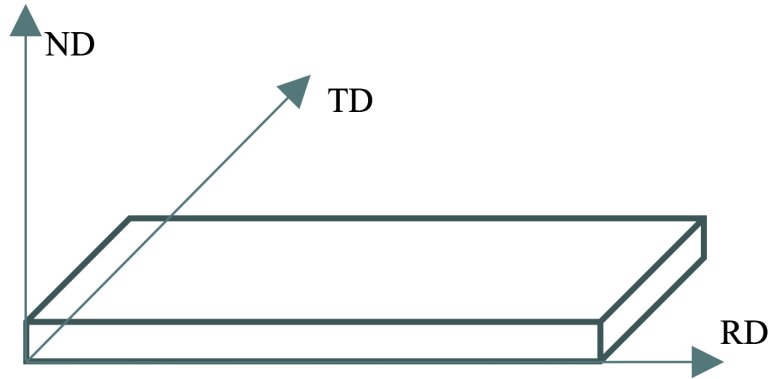


Figure 8: Original matrix shape



Figure 9: SSJ-type tensile specimen: 16x4x0.25 mm

2.2 Microstructural and Mechanical characterization

In order to study the microstructure it has been used a JEOL JXA 8530 scanning electron microscope (SEM), equipped with an electron backscatter diffraction device (EBSD) [43]; the samples have been tested using a SHIMADZU AG-XPlus tester.

For the experiments at room temperature, we have used 3 samples obtained from the TD and 2 from the RD. During the tests the strain rate of the tensile machine has been set as 0.03mm/min; since the tests are at room temperature, the chamber of the machine doesn't need to be depressurized. For the experiments at 673K and 873K, due to the lack of time, only one sample for each direction has been prepared and tested. The data have been recorded through two different type of measurements: the first method recorded the displacement of the rod which tensiones the sample; the second one recorded the elongation of the sample with two sensors on both sides. From the slope of each trend the Young's modulus has been calculated, and compared with the literature in order to validate it.

In the work of Su et al.[65], the theoretical value of the Young's modulus has been evaluated according to the following equation:

$$E = a + b * T + c * T^2 \quad (5)$$

where the coefficients are, respectively, $a=206.2$, $b=0.01148$, and $c=-1.162E-04$, taking also into account that the alloy has a bcc (body centered cubic) microstructure. According to the equation (5), the Young's modulus obtained are reported in table 5:

The value of the Young's modulus obtained from the experimental data resulted is, in most of the cases, sensibly lower than the theoretical ones. There are some reasons that might explain such difference among experimental values and theoretical ones. First of all,

Table 5: Theoretical [65] and experimental values of the Young's modulus

Temperature [K]	Theoretical Young's modulus [GPa]	Experimental Young's modulus [GPa] (RD sample)	Experimental Young's modulus [GPa] (TD sample)
298	199.293	78.493	96.946
673.15	161.274	36.741	20.670
873.15	127.634	21.896	25.337

the evaluation of the slope of the stress-strain curve obtained from the tensile experiments is not the proper method to calculate with a sufficient accuracy the experimental Young's modulus, but there are some other methods that involve different procedures, such as the dynamic one [81], the wave propagation's one [82] and some others. Also, among the iron-based alloys, the ODS steel is one of those characterized by a Young's modulus lower than the calculated one despite its excellent tensile properties. In the end, since the evaluation of the Young's modulus is not object of this study, it seems reasonable to use the comparison between experimental and theoretical Young's modulus only as a criterion to express a quantitative validation of the experimental data.

3 Results

From the experiments we have recorded the trends of the stress-strain curve – shown in figure 10 – and summarized the values of yield stress, ultimate tensile strength (UTS), and total elongation in figures (11) and (12) and in table 6.

Looking at the behaviors of the stress-strain curves we can easily catch some differences. The RD sample, in the average, reported a total elongation sensibly higher than the TD ones – figure 12. For what concerns the yield stress and the UTS, at room temperature the RD sample reported higher values of them; this feature becomes narrow with the increase of temperature, until when, the performances of the TD sample overcome the RD ones (we may also notice it in figure 11). Also, the strain hardening that leads to the UTS from the yield point, and the softening before the necking process are influenced by the temperature: there is a predominance of the first one on the second one at room temperature, but as the experiment's temperature increases, the hardening of the alloy becomes weaker, while the softening process becomes dominant.

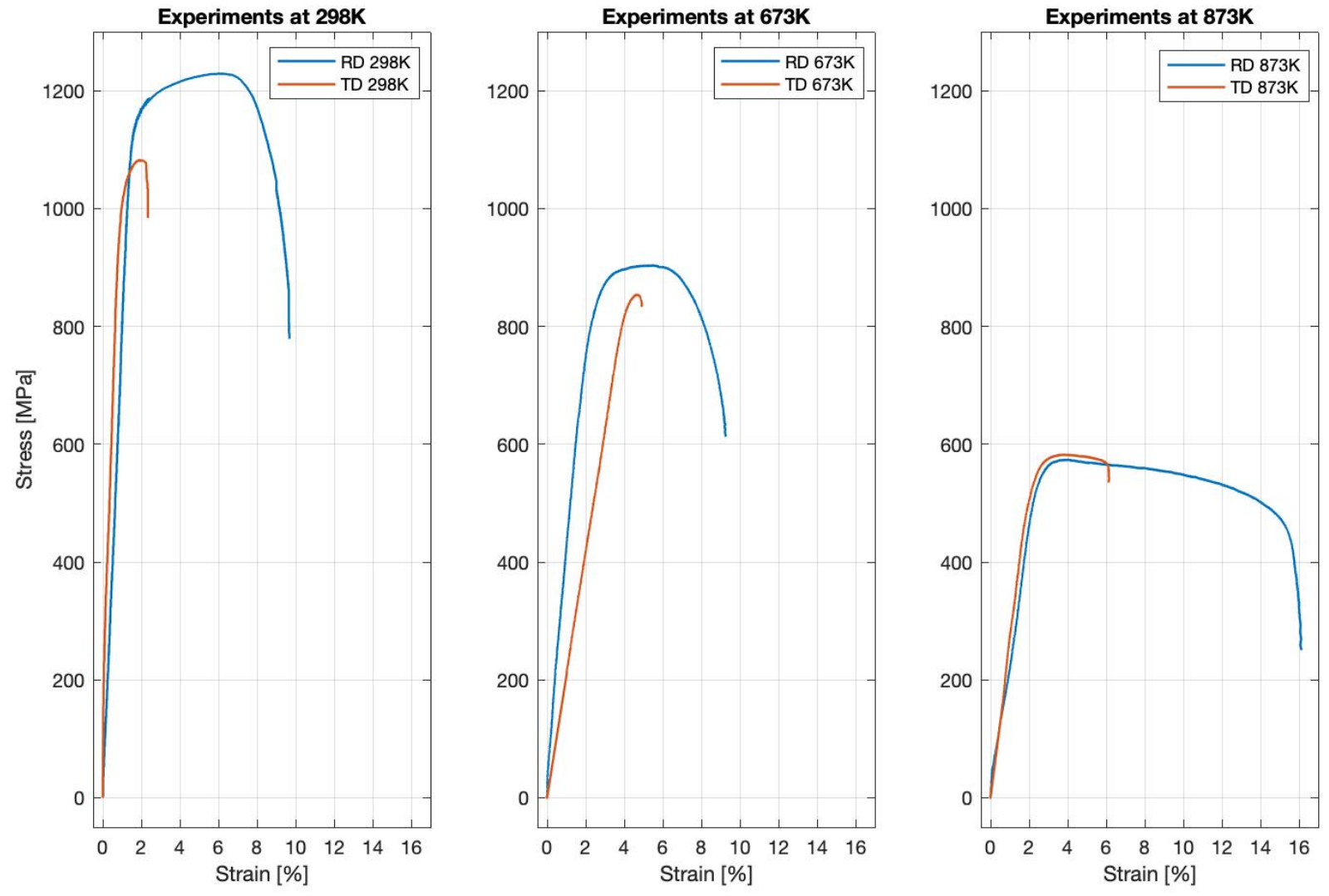


Figure 10: Experimental results of the tensile tests

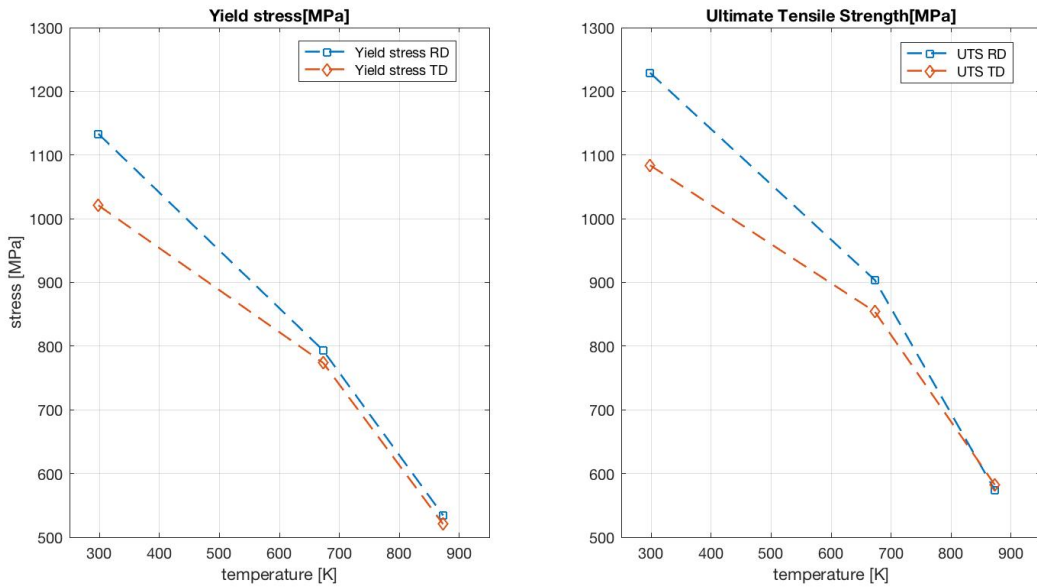


Figure 11: Comparison about yield stress and UTS

Table 6: Experimental values of yield stress , UTS and total elongation

– RD samples

– TD samples

Temperature [K]	Yield stress [MPa]	UTS [MPa]	Total elongation [mm]	Temperature [K]	Yield stress [MPa]	UTS [MPa]	Total elongation [mm]
298	1133.3±17.5	1229.0±23.2	0.186±0.012	298	1021.0±28.1	1083.9±32.6	0.117±0.057
673	798.3	903.8	0.463	673	773.8	854.0	0.277
873	534.3	574.0	0.807	873	520.6	582.30	0.335

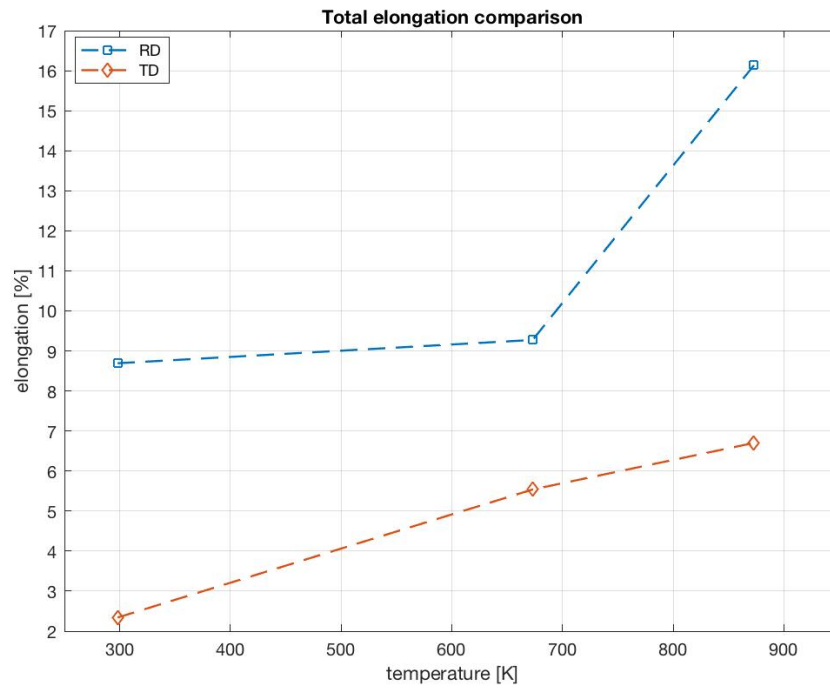


Figure 12: Comparison about total elongation

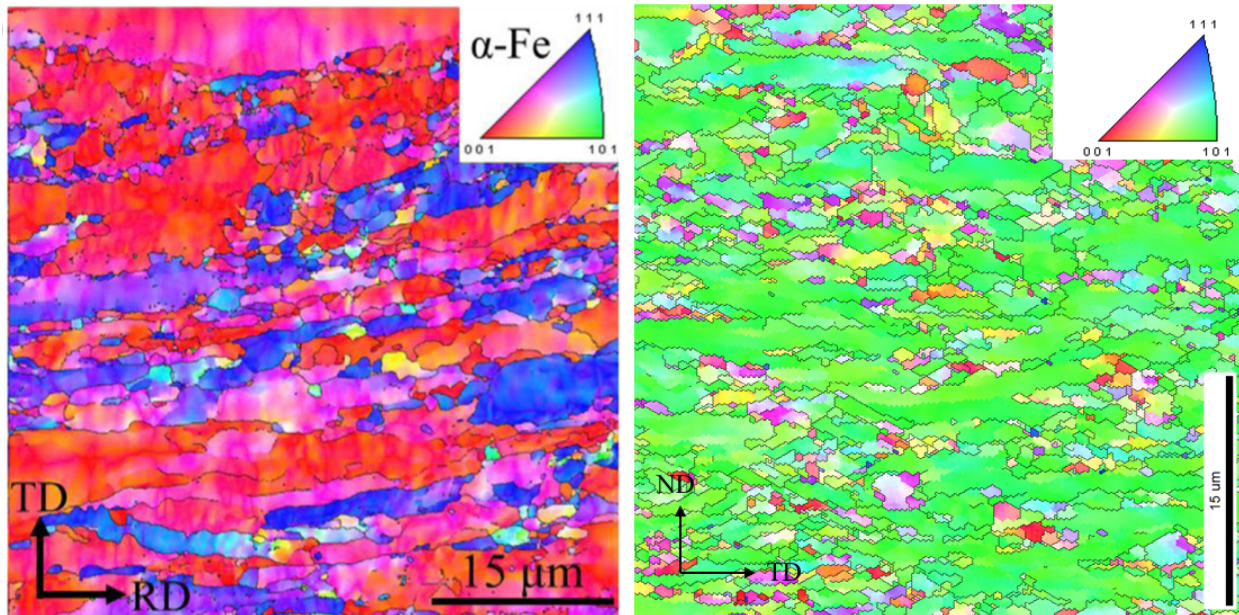
4 Discussion

4.1 Microstructure

Figure 13 shows the inverse pole figures (IPF) of the micro-structure along the RD-TD plane and the ND-TD plane: the characteristic microstructure in RD-TD plane was elongated grains along along the RD direction surrounded by smaller and more equiaxed grains. The grains were preferentially oriented to $\langle 001 \rangle$ (colored as red) and $\langle 111 \rangle$ (colored as blue). The average size ranged from $1\mu\text{m}$ to $8\mu\text{m}$. The annealing and the re-annealing processes below 1383K were observed as trivially effective on the microstructure (even though the temperatures set were, still, enough high) thus the re-crystallization process is not so relevant. In other words the nano-particles have functioned sufficiently to exhibit reasonable integrity against the heat treatments. As a further demonstration of that, a study was conducted with the purpose to investigate the microstructure evolution in an as-fabricated 12Cr ODS steel, and to discuss the coarsening kinetics of Y-Ti-O nanoparticles under annealing at temperature ranging from 1473K to 1673K [68]. It was shown that nanoparticles were very stable during the annealing at 1473K. Also, no significant changes were observed in the microstructure and the texture at 1473K, nevertheless, fully re-crystallization were achieved during the 24h heat treatment at 1673K. They concluded that the re-crystallization in the as-fabricated 12Cr ODS steel did not occur until the dispersoids were still dissolving during the heat treatment. Thus we can esclude that the heating process before the tensile test at 873K did affect the microstructure of the alloy and

eventually its performances. In Figure [13b] we can observe how these grains emerged or deformed in the transverse section, presenting a smaller size, tending to be relatively equiaxed; also they seemed not to be elongated in a preferential orientation. The preferred orientation of the grains is the $\langle 101 \rangle$ (colored as green).

Figure 14 [36] is EPMA analysis data which shows how the particles are distributed in a inhomogeneous way, mainly along the RD direction.



(a) IPF image of the RD-TD plane

(b) IPF image of the ND-TD plane

Figure 13: Inverse Pole Figure (IPF) of the microstructure

SEM characterization of the alloy obtained information about the precipitate morphology and distribution in the matrix and the corresponding EPMA (electro probe microanalyser) map (14b, 14c, 14d) revealed that coarse particles were mainly composed by titanium, carbon and oxygen; their analysis of the XRD (X-ray diffraction) spectra, combined with the EPMA revealed that coarse precipitates were TiC_xO_{1-x} compound, probably due to incomplete milling of Ti raw powders during the mechanical alloying, which reacted with

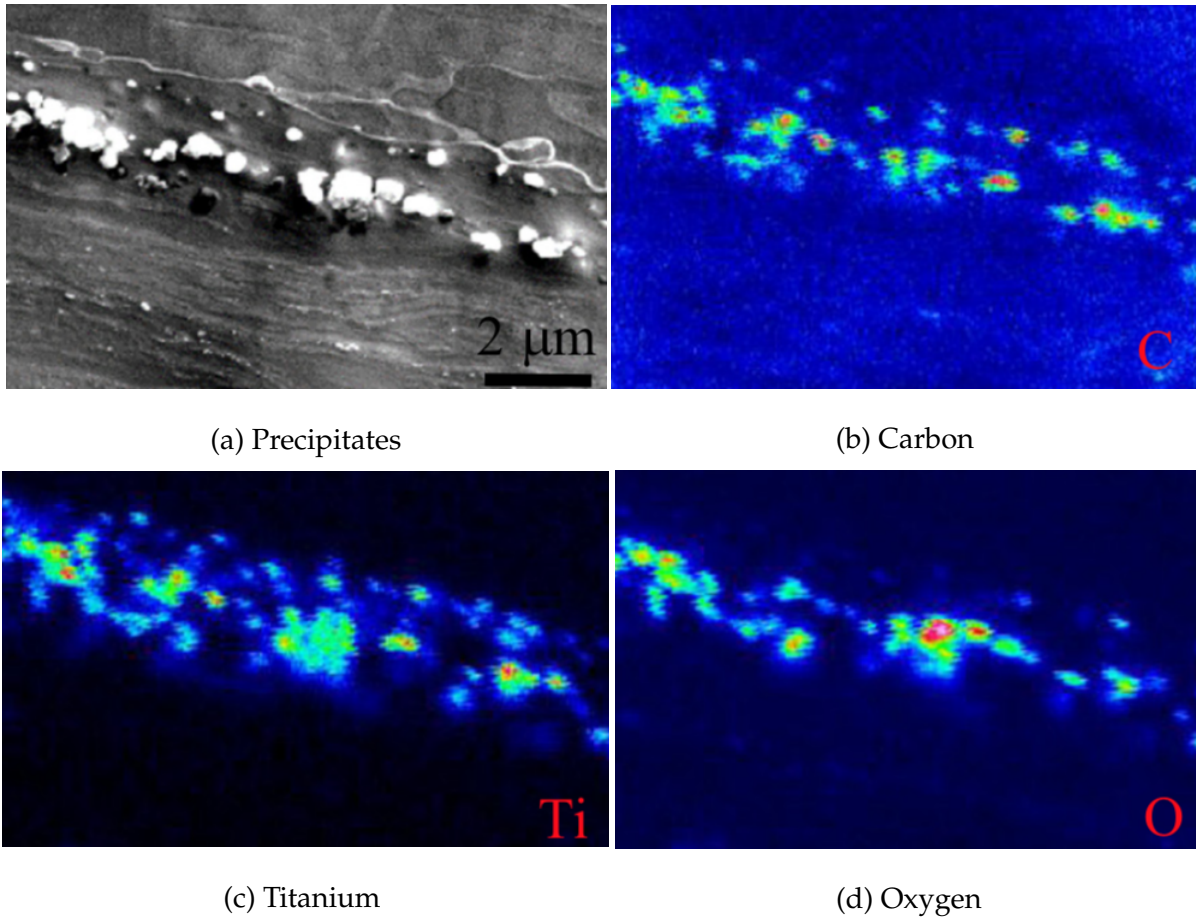


Figure 14: EPMA elemental mapping of coarse precipitates [36]

O and C thanks to their high affinity. Their inhomogeneous distribution is likely due to the hot extrusion and the rolling process.

4.2 Strengthening mechanism

The mechanical properties of the alloy are influenced by some mechanisms related to the microstructure: the nature of the grains and their boundaries, σ_g , the distribution of solid solutes, σ_{ss} , the peculiarity of this kind of alloy – the nanoparticles, σ_p – and also the density of dislocation, σ_{dis} . These microstructure's characteristics affect the mechanical

properties of the alloy in different ways, depending also from the working temperature. Here below they are briefly introduced.

In first approximation the yield stress can be calculated as sum of the already cited terms:

$$\sigma_y = \sigma_0 + \sigma_g + \sigma_{ss} + \sigma_p + \sigma_{dis} \quad (6)$$

In equation (6) the first term, σ_0 , is the friction stress of single crystal, which should be between 50MPa and 60Mpa [45]. The second term, σ_g is related mainly to the grains: if the alloy is characterized by very fine grains, this type of strengthening is not so appreciable. On the contrary if the microstructure is mainly characterized by coarse grains (shorter length of grain boundaries), or there are a lot of impurities and precipitates at the grain boundaries this effect is more relevant [47]. It is usually expressed through the Hall-Petch formula [48,49].

$$\Delta\sigma_g = \frac{\Delta k_{HP}}{\sqrt{D}} \quad (7)$$

The third term, σ_{ss} , is due to the solid solution strengthening. Basically solute atoms provide local strain of the alloy atoms in the host matrix and this hinders the dislocation motion which results in an increase on the strength of the alloy. We can consider negligible the contribution due to carbon and nitrogen because the titanium addition in the alloy limited the dissolution of carbon and nitrogen as interstitial atoms [43]. The same cannot be said about the substitutional strengthening of chromium and tungsten, evaluated as [50,57]:

$$\sigma_{ss} = 0.00689kC^n \quad (8)$$

where k is the strengthening coefficient and it is 1400 for chromium and 11000 for tungsten, while the C is the equilibrium concentration of substitutional elements in atom in percent, and $n=0.75$.

The term σ_p is related to the precipitates strengthening - in this work, yttria dispersoids. The size distribution and volume fraction of the oxide dispersoids can control the grain growth during consolidation and it can also have a relevant impact on the improvement on the creep properties of the consolidated ODS alloys [51,52]. Thanks to their large (negative) heat of formation and high melting point [53], these particles are, thus, very stable at processing and working temperatures. In order to evaluate the σ_p term, the oxide particles have been assumed as impenetrable and the Orowan by-pass mechanism have been used; it is expressed by the Ashby-Orowan equation [54,55]:

$$\sigma_p = \frac{0.8MGB}{2\pi L\sqrt{1-\nu}} \ln \left(\frac{\sqrt{\frac{2}{3}}d_p}{2b} \right) \quad (9)$$

$$L = \sqrt{\frac{2}{3}}d_p \left(\sqrt{\frac{\pi}{4f}} - 1 \right) \quad (10)$$

where ν is the Poisson's ratio assumed to be 0.3, L is the average inter-particle spacing length, f is the volume fraction and d_p the average diameter of particles.

The last term, σ_{dis} , is about strain hardening which is enhanced by plastic deformation. Thanks to the strain hardening the dislocation density increases, as well as their interaction: this will make the dislocation motion much more harder occur and macroscopically will be translated in an increase of the alloy strength at the expenses of the ductility. It can be evaluated using the Bailey-Hirsch relationship [56]:

$$\sigma_{dis} = M\alpha Gb\sqrt{\rho} \quad (11)$$

where M is the Taylor factor estimated as 3.06 for the majority of polycrystalline bcc metals [56], α is assumed to be equal to 0.38 [57,58], G is the shear modulus which for the iron equals to 81.9GPa(44). The term b represents the Burgers vector, it $\sim 0.14371\text{nm}$, and ρ is the dislocation density, $\sim 6.8 \times 10^{14} \text{m}^{-2}$, both of which have been evaluated by Shen et al. in their work[43].

The already mentioned model is not the only one used to explain how the mechanical properties of the alloy are affected by its microstructure characteristics. There are some other models to express this dependency, one of which supposes to sum the terms related to the strain hardening and nanodisperoids through their mean square root. This is reasonable, considering the large concentration of dislocation and nanoparticles in the microstructure [44]: a dislocation density of $\sim 6.8 \times 10^{14} \text{m}^{-2}$ leads to a average dislocation spacing of $\sim 38\text{nm}$, while the average interparticle spacing is $\sim 44\text{nm}$ [43]. Since their spacing lengths are similar, it means that both of them hinder the dislocation motion at the same scale; also, considering that both of the spacing lengths are proportional to the $-\rho^{1/2}$, the effective spacing lengths can be expressed as:

$$\frac{1}{L_{eff}^2} = \frac{1}{L_{dis}^2} + \frac{1}{L_p^2} \quad (12)$$

Hence, they will be summed to the other terms through their mean square root:

$$\sigma_{dis,part}^2 = \sigma_{dis}^2 + \sigma_p^2 \quad (13)$$

and summed to the others, so the equation 6 will have the following form:

$$\sigma = \sigma_0 + \sigma_g + \sigma_{ss} + \sqrt{\sigma_p^2 + \sigma_{dis}^2} \quad (14)$$

4.2.1 Room temperature analysis of the strengthening mechanisms, and comparison with experimental results

At room temperature, each strengthening mechanisms has been evaluated quantitatively, and they are shown below. We already said that σ_0 ranges between 50MPa and 60Mpa, and for iron lattice it has been calculated to be around 53.9MPa [43,46]. The second term, the grain boundary strengthening has a value of 215MPa. The third term, the one due to solute precipitates, σ_{ss} , is equal to 68MPa for chromium and 51.8MPa for tungsten. The fourth one, due to nanoparticles, is equal to $\sigma_p=380$ MPa. The last one, due to the strain hardening, σ_{dis} , at room temperature results to be the main contributor, and is equal to 615.8MPa. Each one of the aforementioned terms is summarized in the table 7, along with the experimental results of the tests:

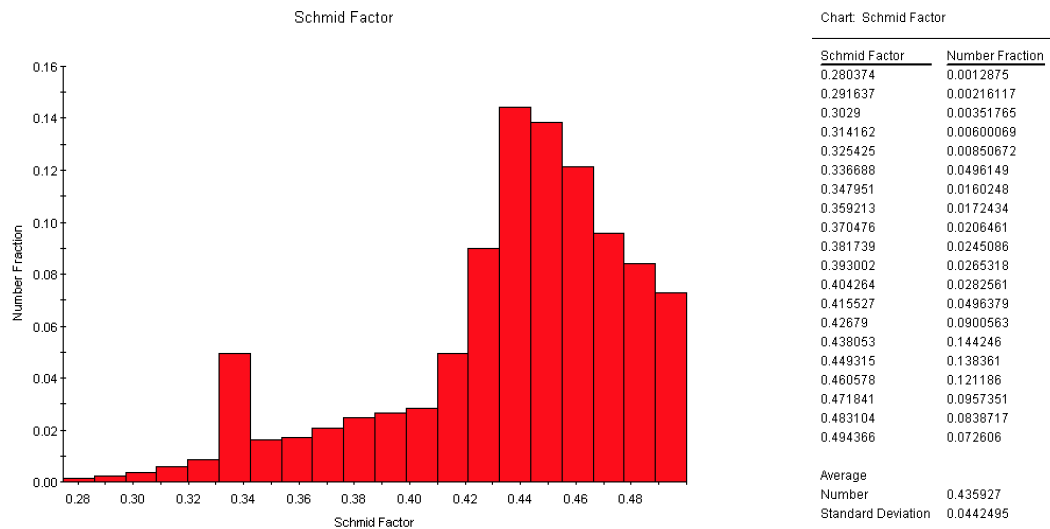
Table 7: Experimental and calculated yield stress [MPa] at RT

σ_0	σ_{gr}	σ_{ss}	σ_p	σ_{dis}	$\sigma_{y,cal}(Eq.(6))$	$\sigma_{y,cal}(Eq.(14))$	$\sigma_{y,exp,TD}$	$\sigma_{y,exp,RD}$
53.9	215	120	380	615.8	1383.3	1111.3	1021.2±28.1	1133.3±17.5

From table 7 we can understand a few things:

- The dominant factors on the strength of the alloy are a high concentration of dislocation (mainly affected by the cold working) and also of yttria dispersoids in the matrix.
- The equation (6) leads to a sensible overestimation of the yield stress of the alloy (around $\sim 30\%$ of error), while equation (14) returns a much better estimation of the experimental values.

- The RD sample has reported a slight higher yield stress than the TD sample, and the same can be said for the ultimate tensile stress (6). This has been confirmed also by the Schmid factor analysis. Briefly, the Schmid factor is related to the slip system of a lattice structure: the shear stress which causes the slip is proportional to the uniaxial stress through the Schmid factor, m (it is the product of the cosine of the angle between the normal to the slip plane and the axial stress, and the cosine of the angle between the slip plane and the axial stress).



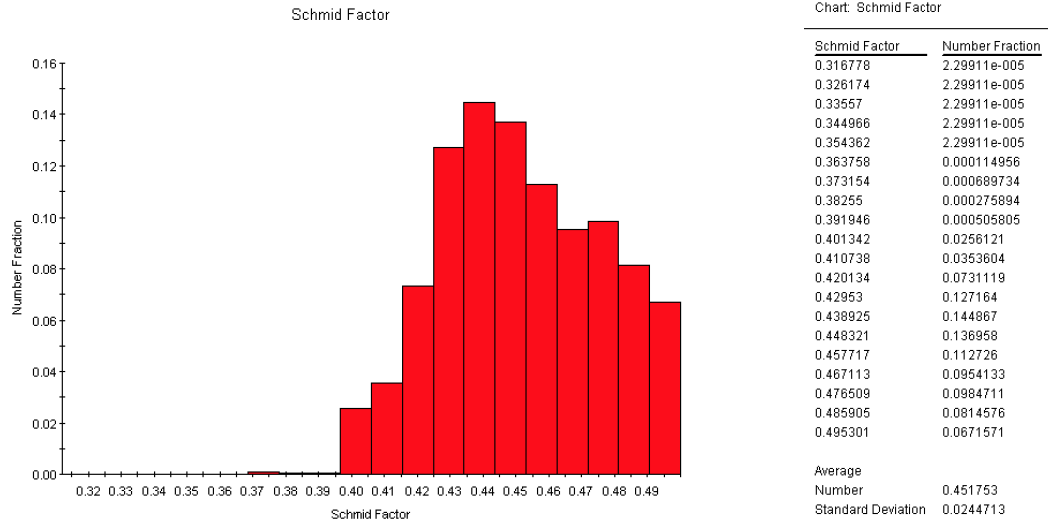
(a) Schmid factor graph for RD sample

(b) Schmid factor values for RD sample

Figure 15: Schmid analysis for the RD sample

The shear stress is maximum when the slip plane is inclined at 45° , and the Schmid factor will be 0.5. The ODS ferritic steel's lattice has a BCC (Body Centre Cubic) structure, so the plane with the highest probability of slip to occur is the $\{110\}\langle -111 \rangle$. Along that plane the Schmid factor for the RD specimen is 0.436 (15b), while for the TD specimen is 0.452 (16b).

$$\tau = \sigma * m \tag{15}$$



(a) Schmid factor graph for TD sample

(b) Schmid factor values for TD sample

Figure 16: Schmid analysis for the TD sample

This barely means that even if the difference between the two Schmid factors is not that high, macroscopically it is translated in a higher external load applied, for the RD samples, in order to cause slip than for the TD samples. Thus, the Schmid factor analysis matches with the results shown in table 6.

4.2.2 High temperature analysis of the strengthening mechanisms

For what concerns the evaluation of the strengthening mechanisms at high temperature, it will be performed quantitatively, focusing the attention only on the type of dependency rather than performing also a numerical evaluation.

We have already said that grain boundaries strengthening mechanism is related to the Hall-Petch effect. Usually, this effect is relevant at low temperature, and that is why most of the studies about it are performed at room temperature. To be more precise, the Hall-Petch effect is relevant at low homologous temperature (the homologous temperature is the ratio

between the temperature of interest and the melting point of the alloy studied), T/T_m . Materials with $T/T_m < 0.2$ will deform athermally at room temperature [66] while for higher homologous temperatures, we observe the Hall-Petch breakdown. Methods to stabilize the grains size, and prevent their growth with the increase of the homologous temperature, do exist, and one of them is to inhibit grain coarsening by pinning the grain boundaries with small particles (precipitates by heat treatments, or dispersoids by mechanical alloying). The alloy object of this study characterized by fine dispersed oxides, the Y_2O_3 , it has a melting point around 1800K [67], so at room temperature, the homologous temperature is ~ 0.165 , thus the alloy behaves athermally. As already said before, no relevant changes were observed in the microstructure neither re-crystallization occurred at 1473K so, it may be assessed that the Hall-Petch effect is still relevant even at 873K, of course in a less sensible way, since the homologous temperature would be ~ 0.43 , but it is hard to expect a drop of its strength because of the temperature set.

Speaking about the dispersed oxides, their influence on the strength of the alloy becomes more relevant at high temperatures since they do not coarsen at very high working temperatures while other strengthening mechanisms have already become weaker. The effects of nanoparticles on the dislocation motion depend on their size and strength; the interaction is described by the Orowan mechanism and the Friedel effect. The formation of precipitation is dependent of the temperature and time and usually occurs discontinuously: while the alloy components first exhibit an irregular distribution, they start to accumulate in preferred position in the matrix as the temperature increases, causing the formation of local superposed structures such as short-range separation, clustering and straining the lattice [74]. If the precipitate is small and not overly hard, it is sheared by the dislocation, as per the Friedel effect to form an antiphase boundary, while if it is hard enough the

dislocation line continues to bend around the particle according to the Orowan mechanism until it is enclosed completely and the dislocation can move on, leaving a dislocation ring around the bypassed particle – image [17]:

However the shearing stress increases proportionally with the square root of the particle' size, and it cannot be higher than the Orowan stress τ_{OW} or the dislocation would require less energy to bow between precipitates.

As we can observe in figure 18, there is a critical radius of the particle that maximizes the shear stress, and usually it ranges between 5nm and 30nm. It is clear that the size of the dispersoids is fundamental for this strengthening mechanism, and it depends also on the heat treatments the al-

loy went through. In the work of Shen et al. [68] they deduced an expression for the coarsening of the dispersed oxides in function of the temperature and time of the heat treatment.

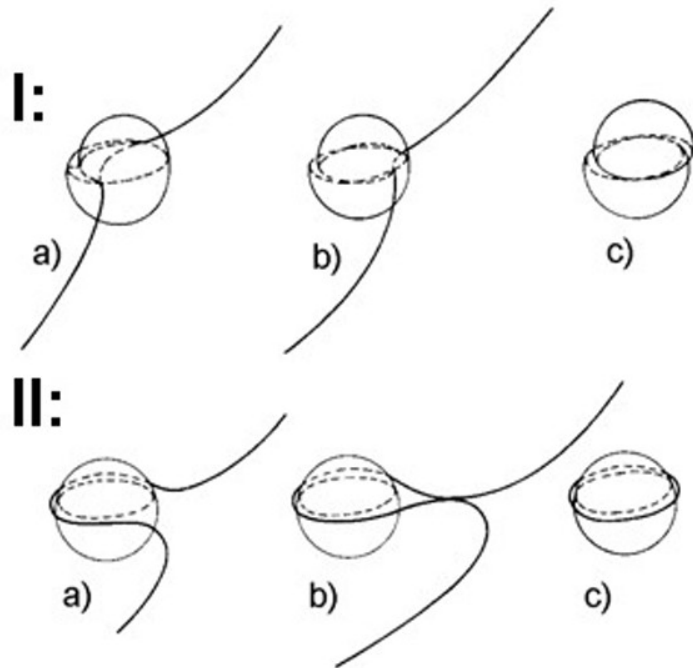


Figure 17: Schematic representation of the Friedel effect (upper sequence – shearing of precipitations) and of the Orowan mechanism (lower sequence – bow-out between precipitations)

$$d_p = \left[1.5 * 10^{15} e^{-\left(\frac{412+55}{8.314T}\right)} t + d_0^3 \right]^{1/3} \quad (16)$$

where T is in Kelvin, t represents the time interval of the treatment, in hours, and d_0 represents the initial average diameter, in nanometer. In one of the heat treatments in their experiments, the alloy was kept at 1473K for 1h: the size of the nanoscale oxides did not changed sensibly and observable also in figure 19a and 19b.

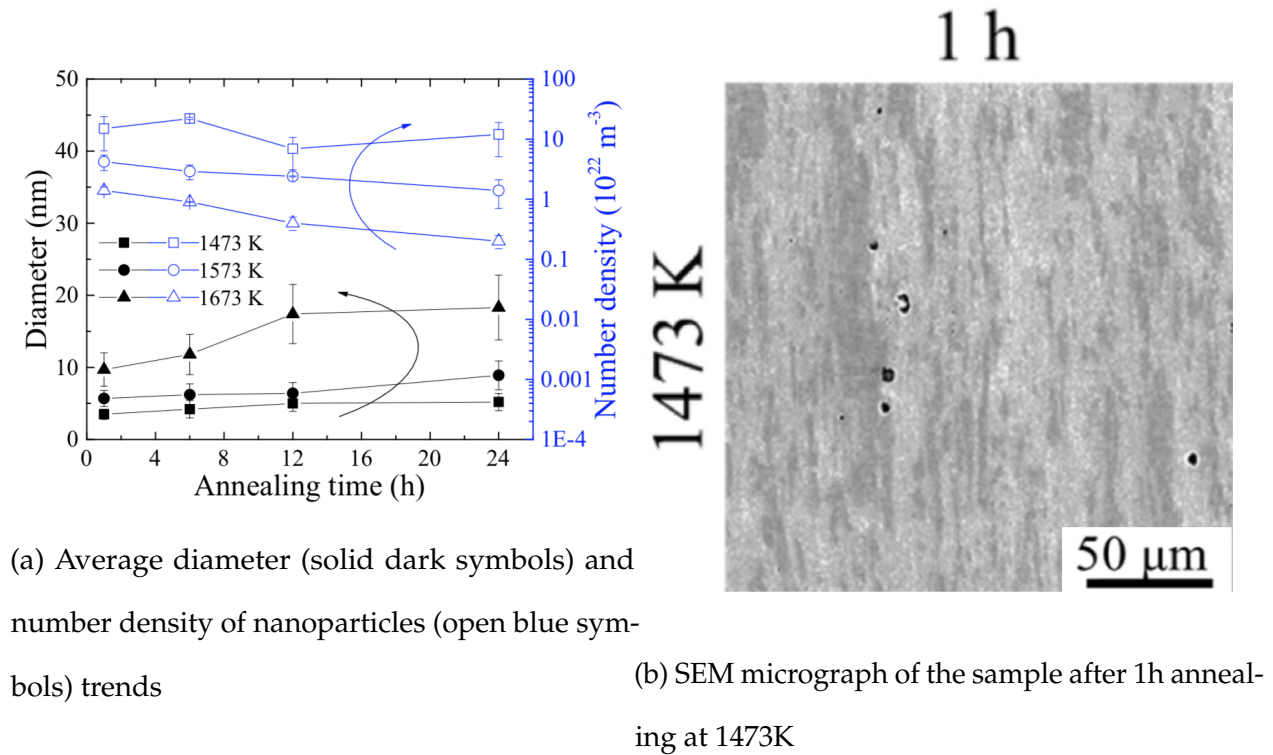


Figure 19: Results obtained during the heat treatments performed in the study of Shen et al. [68]

Acknowledged that the minimum temperature necessary to observe relevant changes in the size of the dispersoids is way higher than the highest temperature set in the experiments performed in this study – 873K – we can deduce that no sensible changes are expected in the growth of the dispersoids. Also, the time interval requested to heat uniformly the sample before the tensile test was around 15 - 20 minutes, (to be conservative we may suppose a heating time of half of hour), so we have reason to think that neither the

temperature nor the time interval of the pre-tensioning heating were not enough high and long, respectively, to enhance the growth of the yttria dispersoids, hence to affect sensibly the precipitates strengthening.

Solid solutes strengthening is characterized by a size misfit of a solute atom in the matrix, causing its strain. In order to describe the behavior of the phenomenon, it is necessary a model which takes into account the actual strengthening effect of the solutes (their concentration), but also the temperature dependence [69]. Another important parameter to consider is the flexi-

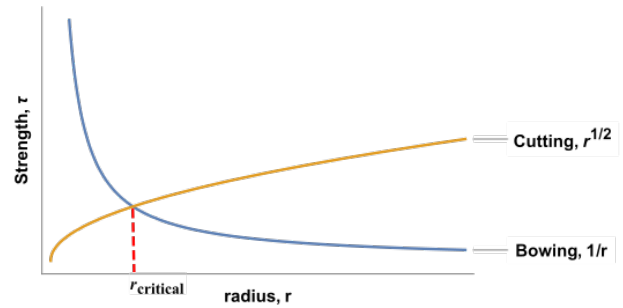


Figure 18: Orowan mechanism: governing behaviors of the precipitation hardening [75]

bility of the dislocation line: two lines are followed in the work of Chandrasekaran, [70]. In the first one [71] a moving dislocation is supposed to go through a series of discrete obstacles on the slip plan, the spacing length of which depends on the flexibility of the dislocation line itself. The second one [72] supposes that resistance to dislocation motion stems from an internal stress, causing the dislocation line to curve, once reached the equilibrium. The discussion so far was made under the implicit assumption of no thermal activation of the dislocation motion, which can occur only at 0 K. Above the absolute zero, thermal activation of dislocation motion has to be considered. Chandrasekaran in its study compared the discrete obstacle model and of two collective models [69, 73] in a graph where the shear stress dependence on the temperature is normalized to the shear stress at 0 K.

The 12Cr ODS steel was tested in a range of temperatures that is not fully shown in

figure 20, but even considering the solid line, its trend decreases way gradually at temperatures far from the absolute zero: this means that above room temperature, the strength of solid solutes does not decrease sensibly. Moreover, the contribution of chromium and tungsten at room temperature are 68MPa and 52MPa, less than one order of magnitude of the yield stress of the alloy, thus, at higher temperatures, it would be harder to appreciate their reduction.

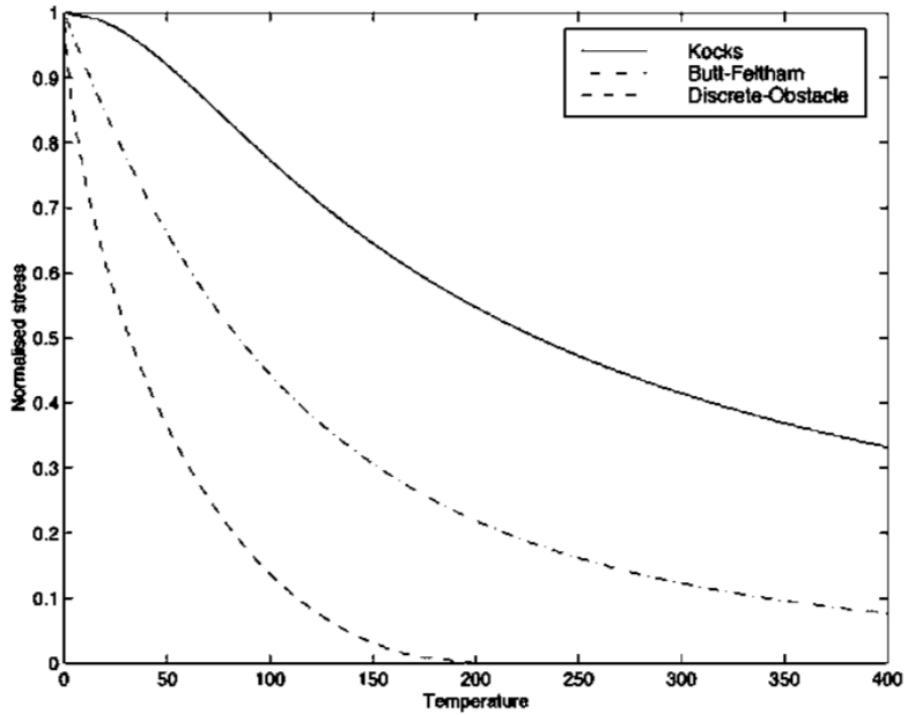


Figure 20: Normalised stress $\frac{\sigma}{\tau}$ as a function of temperature as predicted by a Discrete-Obstacle model – dashed – and two collective models, Butt-Feltham – dott dashed – [73] and Kocks – solid line – [69]

At room temperature, the main source of strength of the alloy is represented by the strain hardening, which causes an increase of dislocation density and it hinders the dislocation motion. Alloys with BCC structure show strong dependence of the yield stress

on the temperature and strain rate: in other words, the overcoming of Peierls-Nabarro barriers is the principal mechanism. At the microscopic scale, the plastic deformation is controlled by generation, motion and interaction of dislocations. Most of the time, macroscopic deformation behavior can be obtained studying the temperature and strain rate dependence of the flow stress, considering the properties of single dislocation [76]. Studies have shown that growth of dislocation density is nearly linear with regard to the deformation in the first steps of the hardening process, independently of the temperature. Then, recombination of dislocation is assumed to be proportionate with the dislocation density itself [77, 80]. Dislocations are supposed to move with an average dislocation velocity v [79] determined through thermal activation by overcoming local obstacles to dislocation motion:

$$v = v_0 * \exp\left(-\frac{G}{kT}\right) \quad (17)$$

k is the Boltzmann constant, T the absolute temperature in K, and G is the shear stress-dependent free energy of activation.

However, in metals, deformation beyond the elastic limit activates and moves its dislocations through the crystal. Two types of obstacles prevent their motions: short-range barriers (dislocation trapping, overcome by introducing thermal energy in the crystal), and long-range barriers (due to the microstructure). Therefore the flow stress can be decomposed in two components, a thermal one, and an athermal one:

$$\sigma = \sigma_{th} + \sigma_{ath} \quad (18)$$

where the first one, σ_{th} is the thermal component, expressed as

$$\sigma_{th} = \sigma_{ts} \left[1 - \left(\beta_1 T - \beta_2 T \ln \frac{\dot{\epsilon}_p}{\dot{\epsilon}_{p0}} \right)^{\frac{1}{q}} \right]^{\frac{1}{p}} \quad (19)$$

where σ_{ts} is the threshold stress at which the dislocations can overcome the barriers without the assistance of thermal activation ($\sigma_{th} = \sigma_{ts}$ where $G = 0.0$), $\dot{\epsilon}_p$ is the equivalent plastic rate, $\dot{\epsilon}_{p0}^i$ is the one at the initial stage, β_1 and β_2 are parameters, and p and q are constants evaluated by Kocks [78]. The athermal one, σ_{ath} is expressed as:

$$\sigma_a = Y_a + \dot{B}(1 - \exp(-k_a \epsilon_p)) \quad (20)$$

where Y_a is related to the microstructure parameters (e.g. D_g , grain diameter), \dot{B} is defined as hardening parameter, and k_a is the dislocation annihilation factor (it depends on both temperature and strain rate). So the total flow stress for bcc metals can be expressed as follow:

$$\sigma = \sigma_{ts} \left[1 - \left(\beta_1 T - \beta_2 T \ln \frac{\dot{\epsilon}_p}{\dot{\epsilon}_{p0}^i} \right)^{\frac{1}{q}} \right]^{\frac{1}{p}} + Y_a + \dot{B}(1 - \exp(-k_a \epsilon_p)) \quad (21)$$

Experimental observations on BCC metals have shown strong dependence of the yield stress by the strain rate and the temperature, while the temperature influence of the plastic hardening and the elongation is weaker, in particular in a range of temperature far from the melting point (it becomes more relevant with the increase of temperature though). As we observed in figures (11) and (12) the yield stress of the alloy is more sensible to the temperature, since it markedly changes as the temperature increases; the same cannot be said with the total elongation, which has a weaker dependence from the temperature. Thus, even though the experiments need of a more solid validation, in first instance we may say that they quantitatively match with the theory. To summarize, the strain hardening which mainly affects the yield stress, decreases visibly with the rising of the temperature, making the alloy more ductile.

4.3 Total elongation and fracture surface

4.3.1 Total elongation analysis

The tensile experiments have shown a sensibly different behavior of the specimens along the RD and the TD in terms of elongation as evident in figure 10. In the case of the sample parallel to the hot extrusion direction, the elongation recorded is larger than twice the one of the TD sample, which thus is less ductile than the previous one. The explanation of such difference could be found in the anisotropy of the microstructure, since the elongated grains, parallel to the rolling direction, are able to better absorb the stress applied by the machine and consequently being deformed; it was observed in another work (the one made by Okada et al. [62]) that grain boundaries seem to slide likely along elongated grains parallel to the cold rolling direction, so it could be a further explanation of such marked difference in the elongation of the RD sample with respect to the TD one. Also, the particles located at some grains boundaries of the elongated grains (as shown in the picture 14a) could act as nucleation points of defects, promoting also the grains boundary sliding in the RD, and limiting the elongation along the TD. Hence, the microstructure characterized by elongated grains in the RD coupled with the presence of small particles in the grain boundaries could justify such evident difference in the elongation of the RD sample with respect to the TD one.

4.3.2 Fracture surface analysis

Both the specimen fracture surfaces have been studied; even from the images at low magnification is possible to observe some difference between the specimens, as shown in figure 21. On the top figure – TD sample – the necking process did not affect the width of the specimen highly enough to cause an appreciable reduction of its cross section area,

at least if we compare this necking process with the one shown in the second line – RD specimen. Even though the magnification is still low, it is clear that the TD specimen presented a more brittle behavior than the RD one as we can also observe in the figure 23. In the second case, both the thickness and the width of the sample appear significantly reduced before the final rupture.

Detailed views of the samples revealed much more information about the phenomena occurred during the necking process of both type of samples. A common thing observed in the surface of the samples in both the directions is the anisotropic fracture behavior and one of the factors that might influenced it is the inhomogeneous distribution of Ti enriched particles (Fig. 14c). Transgranular dimples formation, which was quite often observed on fracture surfaces (Fig. 24), could be caused by void growth and coalescence originating from these Ti enriched particles. The alignment of these particles parallel to rolling direction enhances crack propagation via dimple formation along that direction. Thus TD oriented samples (primary crack propagation towards RD direction) had lower fracture toughness than RD oriented samples and this matches with the less ductile fracture mode occurred on the TD sample.

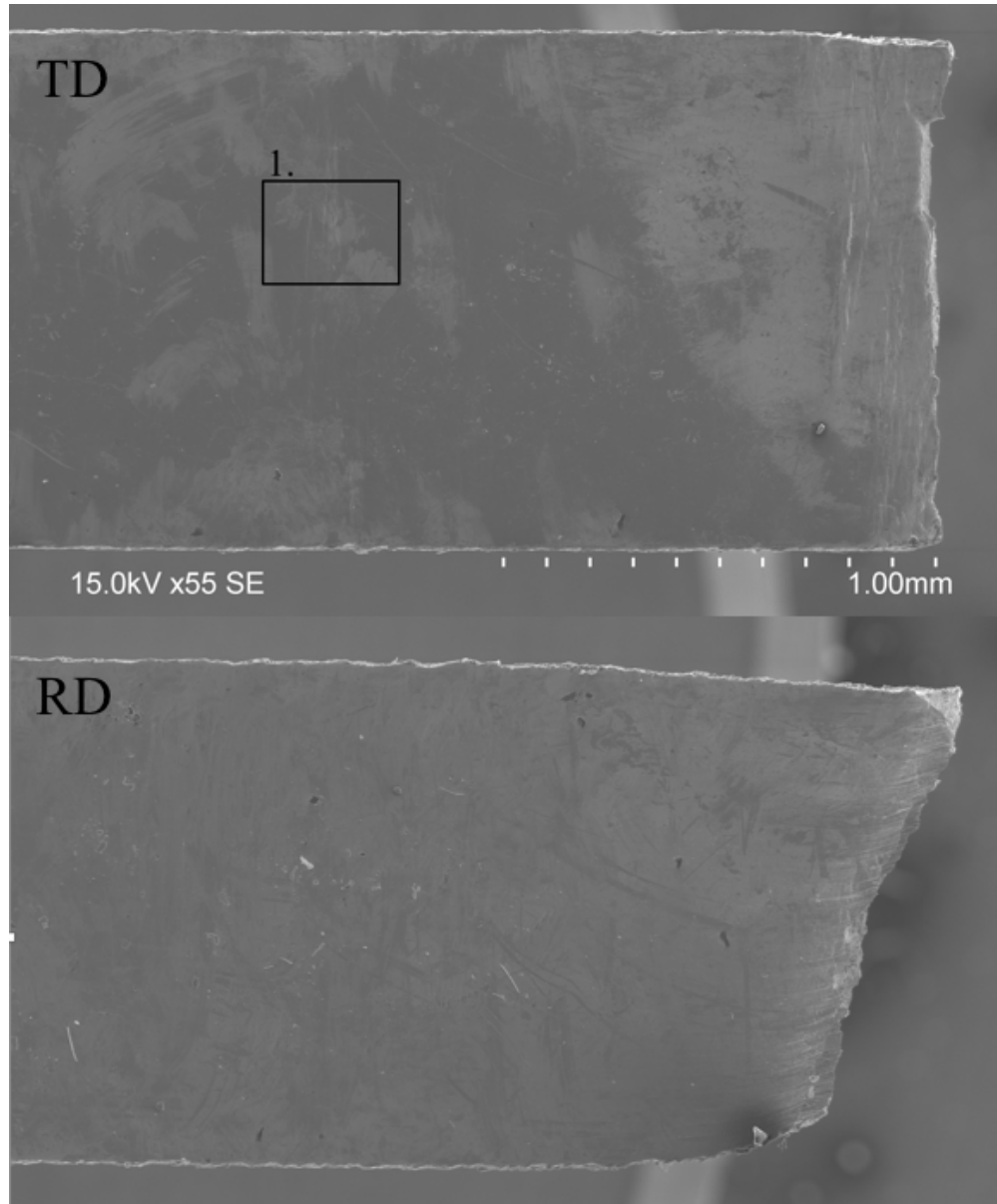


Figure 21: Fracture analysis of the samples – Necking process

On fig. 22 (a zoom of the 21 top) was observed a secondary crack on the surface of the sample caused during the tensile test.

On fig. 24a and 24b we can observe with higher accuracy how the necking process has affected the RD sample surface, ragging the cross section area with stripes until the

collapse of the alloy.

A magnified view of the alloy (25b and 25a) reveals that there are some cleavage facets (possibly formed at the grains boundaries, where cleavage surface tried to change direction to follow the crystallographic cleavage planes of the adjacent crystal) surrounded by fine-structured areas: the last ones are characterized by a lot of dimples (they represent coalesced voids caused by spherical Ti-rich oxide particle, from which cracks could be initiated), [63]. Similar fracture surface has been found in the experiment performed by Ankur Chauhan et al. in their work on a quite similar alloy [64].

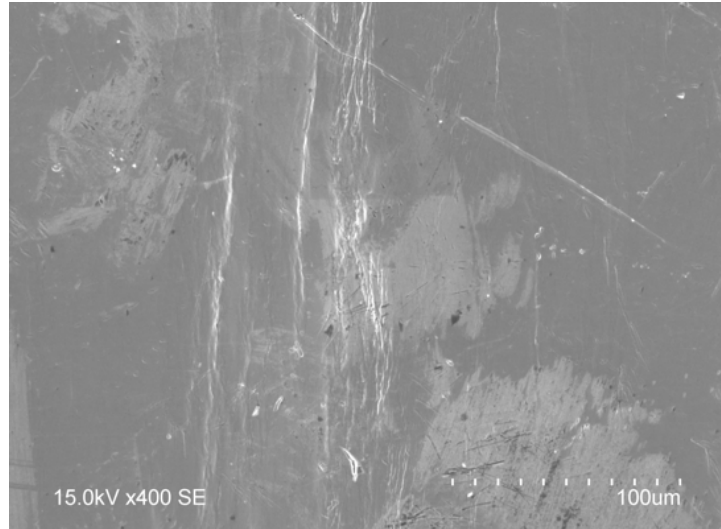


Figure 22: Secondary crack on the TD sample – zoom 1.

The observed mixed mode fracture could be a consequence of the testing temperature, since it is in the range of the ductile to brittle transition temperature of the material – DBTT, which for alloys of similar composition has already been determined to be around 100°C [59, 60]. The ragged fracture could be explained through the bimodal microstructure, composed by smaller and more elongated and larger grains: the smaller grains have low capability to absorb dislocation, thus lower ductility and enhance fracture. The longer ones undergo localized deformation by necking before fracture and this would explain the formation of steps with dimples and cleavage facets. The cause of the crack formation

can be due to the anisotropic microstructure, the strong crystallographic orientation of the small grains along the $\langle 001 \rangle$ and $\langle 111 \rangle$, or even also can be caused by the presence of Ti-rich particles at the grains boundaries.

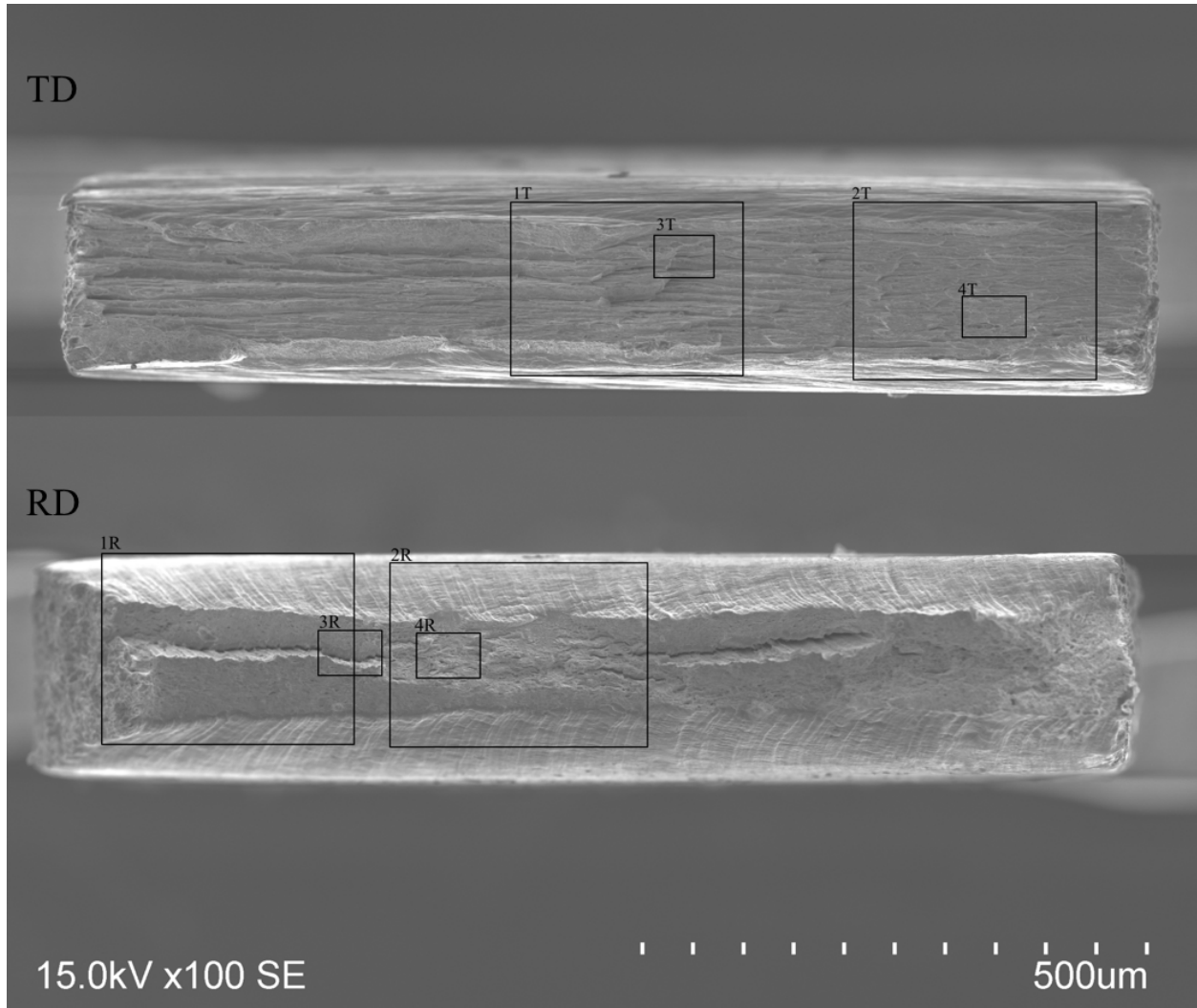
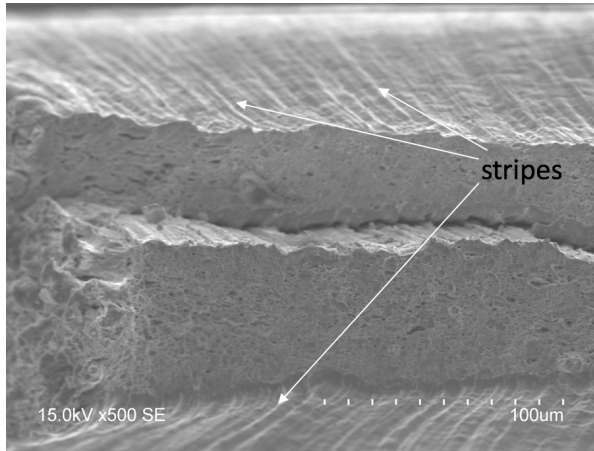


Figure 23: Fracture analysis of the samples – low magnification

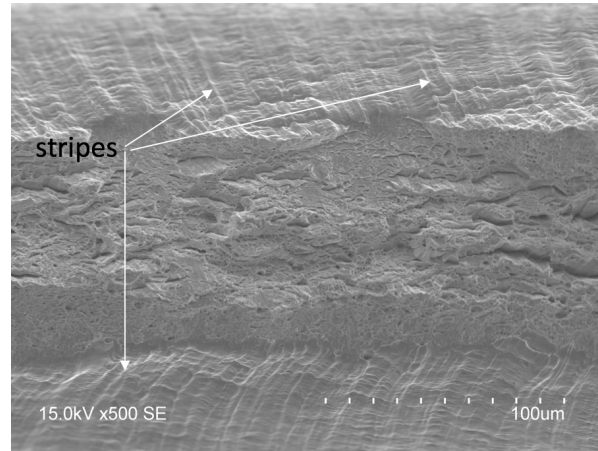
Figures 24c and 24d show at higher magnification the fracture surface of the TD sample: in this case there are much more cleavage facets than on the RD and the dimples found in most of the cases are flat, large and elongated (similar behaviors have been recorded

elsewhere [61]).

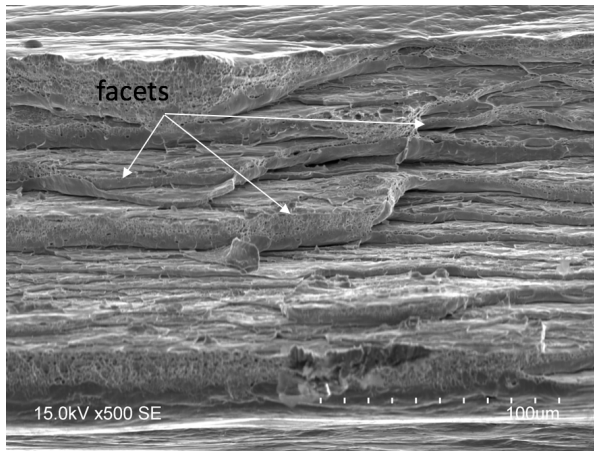
At further high magnification (25c and 25d) we can note intergranular brittle fracture, surrounded by more marked steps: this let us to think about a mixed partially brittle and ductile fracture.



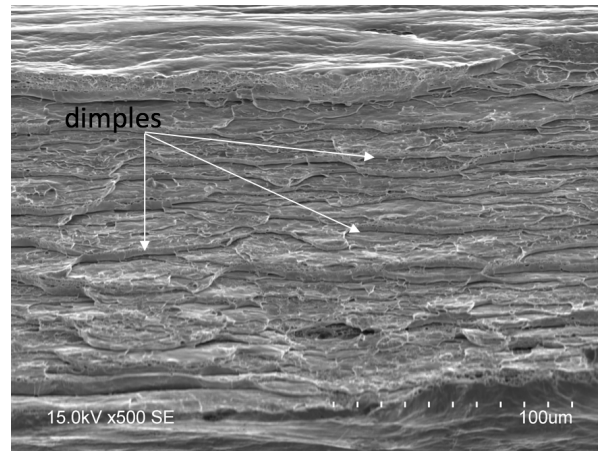
(a) RD sample – zoom 1R



(b) RD sample – zoom 2R



(c) TD sample – zoom 1T

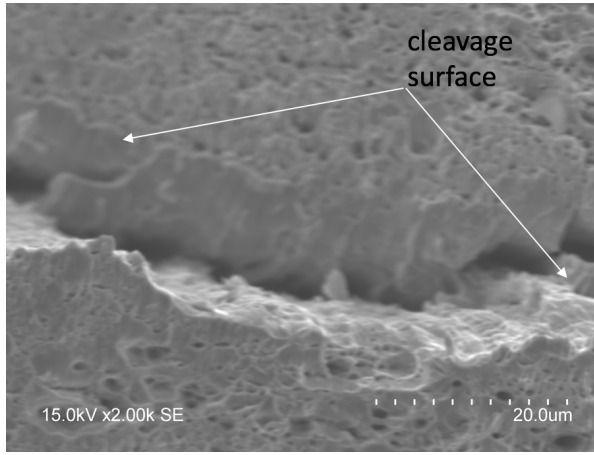


(d) TD sample – zoom 2T

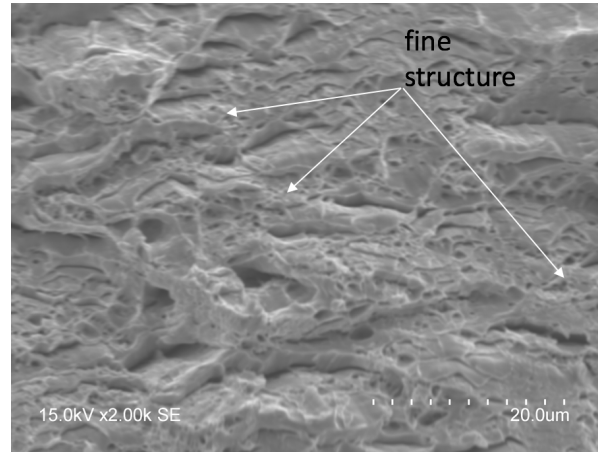
Figure 24: Fracture analysis of the samples – medium magnification

Even for the TD sample, the testing temperature influenced the behavior of the necking process, but considering the observed behavior of the specimen, the DBTT could occur at higher temperature, and this is probably due to the different distribution of the grains

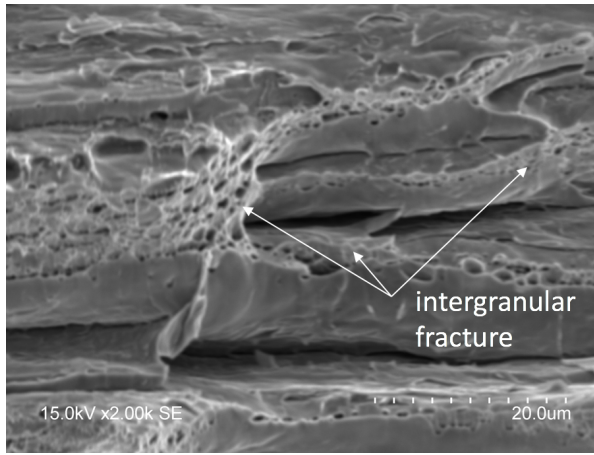
in the TD direction. In another work it has been found that how the microstructure have affected the DBTT range, such as the one of Kasada et al. [22]



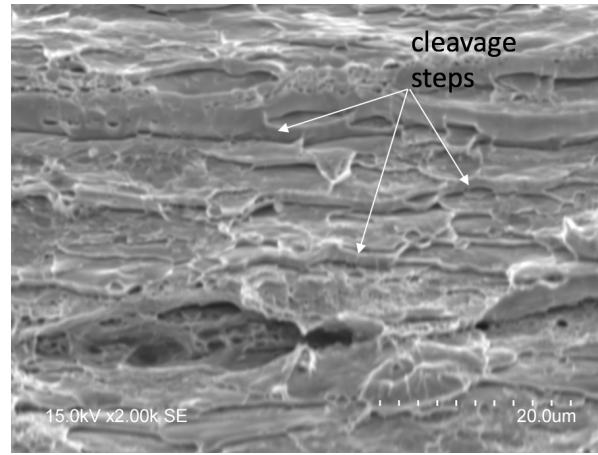
(a) RD sample – zoom 3R



(b) RD sample – zoom 4R



(c) TD sample – zoom 3T



(d) TD sample – zoom 4T

Figure 25: Fracture analysis of the samples – high magnification

We need also to consider the effects of the cold rolling process through which the alloy microstructure has been influenced (more uniformly shaped grains along the transverse direction making the alloy less ductile and elongated grains perpendicular to the specimen, so they are less efficient to absorb energy on transverse direction). This means that during

the test they were not able to absorb the elongation imposed by the machine, so when the stress applied by the machine exceeded the yield one of the alloy, sharp slip of some plans occurred, and this could explain why the dimples observed in the surface are more flat and large than in the case of the RD sample.

5 Conclusions

The 12Cr ODS steel with the nominal composition Fe-12Cr-2W-0.3Ti-0.25Y₂O₃ was obtained through mechanical alloying of base material and yttria powder, hot extrusion, hot forging, cold rolling and final heat treatment. The microstructure has been characterized through SEM, EBSD. The mechanical properties have been tested at room temperature and compared with the expected values from theory. The main conclusions will be reported below:

- The mechanical procedure performed influenced the alloy, and allowed the elongation of the grains along the cold rolling direction (due also to the process itself), while along the transverse direction, the grains have not been influenced enough by the cold rolling process, thus they are more uniform and equiaxed.
- The mechanical properties obtained from the test have shown a yield stress of 1.11GPa and a UTS of 1.20GPa for the RD sample while for the sample in the other direction the already mentioned quantities are respectively of 1.05GPa and 1.13GPa. The performances are slightly better for the RD sample rather than the TD one, but the main difference between the behaviors of the samples along the two direction is the total elongation recorded: the RD sample has shown a more ductile behavior and a total elongation of $\sim 10\%$ which is sensibly larger than the one recorder from the TD sample $\sim 3.5\%$, and this is likely due to the bimodal grain size distribution in the matrix.

- From the experiments at room temperature we can deduce that the presence in the alloy of yttria particles and the hardening occurred during the cold work are the main responsible of the strength of the alloy, while the presence of solid solutes and the grains size did not affect significantly the mechanical properties of the steel.
- At higher temperature the strengthening mechanisms of the alloy have changed differently: the yttria dispersoid have shown the reason why the alloy is regarded to be used in very aggressive environments, since their contribution have not changed that much with the increase of temperature set, thus, at least in the range of temperature investigated, this strengthening mechanism is almost temperature independent. Grain size strengthening and solid solutes strengthening decreased their contribution with the increase of temperature, but they have not brake down. The term due to strain hardening is the one which resulted to be the most affected by the temperature, therefore it is the main reason of the decrease of the strength of the alloy in the range of temperature of interest in this study.
- The fracture surface in both cases has been characterized by the presence of dimples mixed with cleavage steps, and since the experiments have been performed at room temperature, thus in the range of the DBTT (or at least close enough to be affected by) this might affected the results, even if in different proportion. The RD sample has undergone to a more ductile fracture, with a pronounced necking in both the direction of the cross section area, which has been characterized by fine-structured areas. The fracture of the TD specimen presents a more brittle nature and it seems to be occurred without a marked necking. Also, the surface appears full of cleavage facets, alternated to area of intergranular fracture. In both cases, the anisotropy of the microstructure, and the inhomogeneous distribution of the particles have affected

the fracture surface, although in different ways and entities.

References

- [1] <https://www.gen-4.org/gif/jcms/c-9260/public>
- [2] S.J. Zinkle G.S. Was, Materials challenges in nuclear energy
- [3] <https://en.wikipedia.org/wiki/Nuclear-binding-energy>
- [4] S. Glasstone, R. H. Lovberg Controlled Thermonuclear Reactions, Robert E. Krieger Publishing Copany 1975
- [5] <https://www.nextbigfuture.com/2016/05/international-tokamak-fusion-project.html>
- [6] Hans – Stephan Bosh, Review on Data and Formulas for Fusion Cross-section (1990)
- [7] T. Muroga M. Gasparotto S. J. Zinkle, Overview of materials research for fusion reactors, Fusion Engineering and Design Volumes 61–62,(2002), 13-25
- [8] N. Baluc, K. Abe, J.L. Boutard, V.M. Chernov, E. Diegele, S. Jitsukawa, A. Kimura, R.L. Klueh, A. Kohyama, R.J. Kurtz, Status of R&D activities on materials for fusion power reactors, 2007, Nuclear Fusion, Volume 47, Number 10.
- [9] R.L. Klueh, Cr-Mo steel for fusion reactors first wall- a review, Nucl. Eng. Des. 72(1982) 329-344
- [10] R.L. Klueh, E.E. Bloom, The development of ferritic steel for fast induced-radioactivity decay for fusion reactor applications, Nucl. Eng. Des. Fusion 2(1985) 383-289

- [11] R.L. Klueh, D.S. Gelles, T.A. Lecztenberg, Development of ferritic steels for reduced activation: The US program, *J. Nucl. Mater.* 141(1986) 1081-1087
- [12] F. Abe, T. Noda, M. Okada, Optimum alloy compositions in reduced activation martensitic 9Cr steel for fusion reactor, *J. Nucl. Mater.* 195(1992) 51-67
- [13] F. Abe, T. Noda, H. Araki, S. Nakazawa, Alloy composition selection for improving strength and toughness of reduced activation 9Cr-W steels, *J. Nucl. Mater.* 179(1991), 663-666
- [14] S. Ukai, M. Fujiwara, Perspective of ODS alloys application in nuclear environments, *J. Nucl. Mater.* 307-311(2002) 749-757
- [15] R.L. Klueh, J.P. Shingledecker, R.W. Swindeman, D.T. Hoelzer, Oxide dispersion-strengthened steels: A comparison of some commercial and experimental alloys, *J. Nucl. Mater.* 341(2005) 103-114.
- [16] J.S. Benjamin, Dispersion strengthened superalloys by mechanical alloying, *Metallurgical Transactions* 1 (1970)
- [17] S. Ukai, M. Harada, H. Okada, M. Inoue, S. Nomura, S. Shikamura, K. Asabe, T. Nishida, M. Fujiwara, Alloying design of oxide dispersion strengthened ferritic steel for long life FBRs core material, *J. Nucl. Mater.* 204(1993) 65-73
- [18] T. Narita, S. Ukai, B. Leng, S. Ohtsuka, T. Kaito, Characterization of recrystallization of 12Cr and 15Cr ODS ferritic steels, *J. Nucl. Sci. Technol* 50(2013) 314-320
- [19] T. Hayashi, P.M. Sarosi, J.H. Schneibel, M.J. Mills, Creep response and deformation processes in nanocluster-strengthened ferritic steel, *Acta Mater.* 56 (2008) 1407-1416

- [20] A. Kimura, H.-S. Cho, N. Toda, R. Kasada, K. Yutani, H. Kishimoto, N. Iwata, S. Ukai, M. Fujiwara, High burnup fuel cladding materials R&D for advanced nuclear systems: nano-sized oxide dispersion strengthening steels, *J. Nucl. Sci. Technol.* 44(2007) 323-328
- [21] M. Serrano, A. García-Junceda, M. Hernández (2014) Microstructural anisotropy effect on the mechanical properties of a 14Cr ODS steel, *J. Nucl. Mater.* 428(2012) 103-109
- [22] R. Kasada, S.G. Lee, J. Isselin, J.H. Lee, T. Omura, A. Kimura, T. Okuda, M. Inoue, S. Ukai, S. Ohnuki, T. Fujisawa, F. Abe, Anisotropy in tensile and ductile-brittle transition behavior of ODS ferritic steels *J. Nucl. Mater.* 417 (2011) 180-184
- [23] S. Ukai, M. Harada, H. Okada, M. Inoue, S. Nomura, S. Shikamura, K. Asabe, T. Nishida, M. Fujiwara, Alloying design of oxide dispersion strengthened ferritic steel for long life FBRs core material, *J. Nucl. Mater.* 204(1993) 65-73
- [24] R.L. Klueh, P. J. Maziasz, I.S. Kim, L. Heatherly, D.T. Hoetzeler, N. Hashimoto, E.A. Kenik, K. Miyahara, Tensile and creep properties of an oxide dispersion strengthened ferritic steel, *J. Nucl. Mater.* 307-311(2002) 773-777
- [25] M.C. Brandes, L. Kovarik, M.K. Miller, G.S. Daehn, M.J. Mills, Creep behavior and deformation mechanism in a nanocluster strengthened ferritic steel, *Acta Mater.* 60(2012) 1827-1839
- [26] F.R Larson, J. Miller, A time-temperature relationship for rupture and creep stresses, *Trans. ASME* 74(1952) 765-775
- [27] M. K. Miller, D.T. Hoelzer, Effect of neutron irradiation on nanoclusters in MA957 ferritic alloys, *J. Nucl. Mater.* 418(2011) 307-310

- [28] J. Chen, P. Jung, T. Rebac, F. Duval, T. Sauvage, Y. de Carlan, M.F. Barthe, Helium effects on creep properties of Fe-14CrWTi ODS steel at 650°C, *J. Nucl. Mater.* 453(2014) 253-258
- [29] J. Ribis, Y. de Carla, Interfacial strained structure and orientation relationships of nano sized oxide particles deduced from elasticity-driven morphology in oxide dispersion strengthened materials, *Acta Mater.* 60 (2012), 238-252
- [30] M. Ohnuma, J. Suzuki, S. Otsuka, S.W. Kim, T. Kaito, M. Inoue, H. Kitazawa, A new method for the quantitative analysis of the scale and composition of nano sized oxide in 9Cr-ODS steel, *Acta Mater.* 57(2007) 5571-5581
- [31] S. Yamashita, S.Ohtsuka, N. Akasaka, S. Ukai, S. Onuki, Formation of nanoscale complex oxide particles in mechanically alloyed ferritic steel, *Philos. Mag. Lett.* 84(2004) 525-529
- [32] H. Kishimoto, R. Kasada, O. Hashitomi, A. Kimura, Stability of Y-Ti complex oxides in Fe-16Cr-0.1Ti ODS ferritic steel beforehand after heavy ion irradiation, *J. Nucl. Mater.* 386-388 (2009), 533-536
- [33] P. Unifantowicz, T. Plocinski, C.A. Williams, R. Schäublin, N. Balux, Structure of complex oxide nanoparticles in a Fe-14Cr2W0.3Ti0.3Y₂O₃ ODS RAF steel, *J. Nucl. Mater.* 442 (2013) S158-S163
- [34] C.Y. Lu, Z. Lu, R. Tie, C.M. Liu, L.M. Wang, Microstructure of a 14Cr ODS ferritic steel before and after helium ion implantation, *J. Nucl. Mater.* 455 (2014) 366-370
- [35] M.K. Miller, C.M. Parish, Q. Li, Advanced oxide dispersion strengthened and nanostructure ferritic alloys, *Mater. Sci. Technol.* 29 (2013) 1174-1178

- [36] Yanfen Li, Jingjie Shen, Feng Li a, Huilong Yang, Sho Kano, Yoshi Matsukawa, Yuhki Satoh, Haiying Fu, Hiroaki Abe, Takeo Muroga, Effects of fabrication processing on the microstructure and mechanical properties of oxide dispersion strengthening steels, *Materials Science & Engineering A* 654 (2016) 203-212
- [37] Y. Wu, E.M. Haney, N. J. Cunningham, G.R. Odette, Transmission electron microscopy characterization of the nano features in nanostructured ferritic alloy MA957, *Acta Mater.* 60(2012) 3456-3468
- [38] M. Song, C. Sun, J. Jang, T.K. Kim, K.T. Hartwig, X. Zhang, Microstructure refinement and strengthening mechanism of a 12Cr ODS steel processed by equal channel angular extrusion, *J. Alloy Compd.* 577(2013) 247-256
- [39] J.H. Schneibel, M. Heilmairer, W. Blum, G. Hasemann, T. Shanmugasundaram, Temperature dependence of the strength of fine- and ultra fine- grained material, *Acta Mater.* 59(2011) 1300-1308,
- [40] J.H. Kim, T.S. Byun, T.D. Hoelzer, C.H. Park, J.T. Yeom, J.K. Hong, Temperature dependence of strengthening mechanisms in the nanostructured ferritic alloy 14YWT - Part II - Mechanistic models and predictions, *Mater. Sci. Eng., A*559(2013) 111-118
- [41] J.H. Schneibel, C.T. Liu, D.T. Hoelzer, M.J. Mills, P. Sarosi, T. Hayashi, U. Wendt, H. Heyse, Development of porosity in an oxide dispersion-strengthened ferritic alloy containing nanoscale oxide particles, *Scripta Mater.* 57(2007) 1040-1043
- [42] C.A. Williams, G.D.W. Smith, E.A. Marquis, The effect of Ti on the coarsening behavior of oxygen-rich nanoparticles in oxide-dispersion-strengthened steels after annealing at 1200°C, *Scripta Mater.* 67(2012) 108-111

- [43] J. Shen, Y. Li, F. Li, H. Yang, Z. Zhao, S. Kano, Y. Matsukawa, Y. Satoh, H. Abe, Microstructural characterization and strengthening mechanisms of a 12Cr-ODS steel, *Materials Science & Engineering A* 673 (2016) 624-632
- [44] N. Kamikawa, K. Sato, G. Miyamoto, M. Murayama, N. Sekido, K. Tsuzaki, T. Furuhara, Stress-strain behavior of ferrite and bainite with nanoprecipitation in low carbon steels, *Acta Mater.* 83 (2015) 383-396.
- [45] S. Takaki, D. Akama, N. Nakada, T. Tsuchiyama, Effect of grain boundary segregation of interstitial elements on Hall-Petch coefficient in steels, *Mater. Trans.* 55 (2014) 28-34.
- [46] F.B. Pickering, *Physical Metallurgy and the Design of Steels*, Applied Science Publishers, London, 1978.
- [47] M. I. Gol'dshtein B. M. Bronfin A. Z. Shifman V. V. Osipov Mechanism of grain boundary strengthening of steels, (1979) 104-109
- [48] E.O. Hall, The deformation and ageing of mild steel, *Proc. Phys. Soc. B* 64 (1951) 747-753.
- [49] N.J. Petch, The cleavage strength of polycrystals, *J. Iron Steel Inst.* 174 (1953) 25-28.
- [50] C.E. Lacy, M. Gensamer, The tensile properties of alloyed ferrites, *Trans. Am. Soc. Met.* 32 (1944) 88.
- [51] M. Heilmaier, B. Reppich *Metall. Mater. Trans. A*, 27 (1996), pp. 3861-3869
- [52] J. Weertman, in: J.C.M. Li, A.K. Mukherjee (Eds.), *Rate Processes in Plastic Deformation of Materials*, ASM, Metals Park, OH, 1975, pp. 315-336.
- [53] G.R. Odette, D.T. Holezer, *J. Met.* 62 (2010) 84-92.

- [54] M.F. Ashby, Oxide dispersion strengthening, Godon And Breach, New York,1958.
- [55] T. Gladman, Precipitation hardening in metals, Mater. Sci. Technol. 15 (1999) 30-36.
- [56] R.E. Stoller, S.J. Zinkle, On the relationship between uniaxial yield strength and resolved shear stress in polycrystalline materials, J. Nucl. Mater. 283-287 (2000) 349-352.
- [57] Q. Li, Modeling the microstructure-mechanical property relationship for a 12Cr-2W-V-Mo-Ni power plant steel, Mater. Sci. Eng. A 361 (2003) 385-391.
- [58] A.S. Keh, Work hardening and deformation sub-structure in iron single crystals deformed in tension at 298 K, Philos. Mag. 12 (1965) 9-30.
- [59] M.A. Sokolov, D.T. Hoelzer, R.E. Stoller, D.A. McClintock, J. Nucl. Mater 367e370 (2007) 213.
- [60] R. Rahmanifard, H. Farhangi, A.J. Novinrooz, S. Moniri, Metall. Mater. Trans. A 44 (2012) 990.
- [61] T.S. Byun, J.H. Kim, J.H. Yoon, D.T. Hoelzer, High temperature fracture characteristics of a nanostructured ferritic alloy (NFA), J. Nucl. Mater 407 (2010) 78-82, <http://dx.doi.org/10.1016/j.jnucmat.2010.09.031>.
- [62] H. Okada, S. Ukai, M. Inoue, J. Nucl. Sci. Technol. 33 (1996) 936-943.
- [63] M.S. Oskooie, H. Asgharzadeh, IOP Conf, Ser. Mater. Sci. Eng. 63 (2014) 012022.
- [64] Ankur Chauhan, Dimitri Litvinov, Jarir Aktaa, High temperature tensile properties and fracture characteristics of bimodal 12Cr-ODS steel, Journal of Nuclear Materials 468 (2016) 1-8

- [65] Di Su, Yan-Lin He, Ji-Qiong Liu, Xiao-Gang Lu, Establishment of the Elastic Property Database of Fe-base Alloys, Atlantis Press (2015)
- [66] J. H. Schneibel, M. Heilmaier, Materials Transactions, Vol. 55, No. 1 (2014) pp. 44 to 51
- [67] A. Hirata, T. Fujita, Y. R. Wen, J. H. Schneibel, C. T. Liu & M. W. Chen, Atomic Structure of Nanoclusters in Oxide-Dispersion-Strengthened Steels, Nature Mat. 10, 922 (2011).
- [68] J. Shen, H. Yang, Y. Li, S. Kano, Y. Matsukawa, Y. Satoh, H. Abe, Microstructural stability of an as-fabricated 12Cr-ODS steel under elevated-temperature annealing, Journal of Alloys and Compounds 695 (2017) 1946-1955
- [69] Kocks, U. F. (1985). "Kinetics of Solution Hardening." Met. Trans 16A(December): 2109 - 2129.
- [70] D. Chandrasekaran, Grain Size and Solid Solution Strengthening in Metals, Materials Science and Engineering, A309-310, (2001) 184-189
- [71] Fleischer, R. L. and W. R. H. Jr. (1963). Solution Hardening. Relation of Structure to Mechanical Properties of Metals
- [72] Mott, N. F and F.R.N Nabarro (1948). Dislocation Theory and Transient Creep, Bristol, Physical Society
- [73] Butt, M. Z. and P. Feltham (1993). "Review of Solid-solution Hardening." Journal of Materials Science 28: 2557.
- [74] Bargel, H.J.; Schulze, G. (ed.): Werkstoffkunde; 10. edition, Springer Verlag, Berlin, Heidelberg, 2008

- [75] https://en.wikipedia.org/wiki/Precipitation_hardening
- [76] G. Z. VOYIADJIS, F. H. ABED, Effect of dislocation density evolution on the thermo-mechanical response of metals with different crystal structures at low and high strain rates and temperatures, *Arch. Mech.*, 57, 4, pp. 299-343, Warszawa 2005.
- [77] Bammann, D.J., A model of crystal plasticity containing a natural length scale, *Material Sciences and Engineering A* 309–310, 406–410, 2001
- [78] Kocks, U.F., Realistic constitutive relations for metal plasticity, *Material Science and Engineering*, A317, 181–187, 2001
- [79] Bammann, D.J., Aifantis, E.C., On a proposal of continuum with microstructure, *Acta Mechanica* 45, 91–125, 1982
- [80] Barlat, F., Glazov, M.V., Brem, J.C., Lege, D.J., A simple model for dislocation behavior, strain and strain rate hardening evolution in deforming aluminum alloys, *International journal of Plasticity*, 18, 919–939, 2002
- [81] K. D. Baveja, Dynamic method of measuring Young's modulus of elasticity, 1964 *J. Sci. Instrum.* 41 662
- [82] Achenbach, J. D., *Wave propagation in Elastic Solids*, North-Holland, Amsterdam, 1984